T.R.

GEBZE TECHNICAL UNIVERSITY

GRADUATE SCHOOL OF NATURAL AND APPLIED SCIENCES

QUASI-STATIC FINITE-DIFFERENCE TIME-DOMAIN SIMULATION OF A PULSE INDUCTION METAL DETECTOR

TALHA SAYDAM

A THESIS SUBMITTED FOR THE DEGREE OF

MASTER OF SCIENCE

DEPARTMENT OF ELECTRONICS ENGINEERING

GEBZE

2018

T.R.

GEBZE TECHNICAL UNIVERSITY

GRADUATE SCHOOL OF NATURAL AND APPLIED SCIENCES

QUASI-STATIC FINITE-DIFFERENCE TIME-DOMAIN SIMULATION OF A PULSE INDUCTION METAL DETECTOR

TALHA SAYDAM

A THESIS SUBMITTED FOR THE DEGREE OF

MASTER OF SCIENCE

DEPARTMENT OF ELECTRONICS ENGINEERING

THESIS SUPERVISOR

PROF. DR. SERKAN AKSOY

GEBZE

2018

T.C.
GEBZE TEKNİK ÜNİVERSİTESİ
FEN BİLİMLERİ ENSTİTÜSÜ

DARBE İNDÜKSİYONLU BİR METAL DEDEKTÖRÜNÜN KUVAZİ-STATİK ZAMAN-UZAYI SONLU-FARKLAR BENZETİMİ

TALHA SAYDAM
YÜKSEK LİSANS TEZİ
ELEKTRONİK MÜHENDİSLİĞİ ANABİLİM DALI

DANIŞMANI
PROF. DR. SERKAN AKSOY

GEBZE
2018

GEBZE TEKNİK ÜNİVERSİTESİ	YÜKSEK LİSANS JÜRİ ONAY FORMU

GTÜ Fen Bilimleri Enstitüsü Yönetim Kurulu'nun 27.../.06../...2018 tarih ve 2018../..33... sayılı kararıyla oluşturulan jüri tarafından 23.../.07../2018 tarihinde tez savunma sınavı yapılan Talha Saydam'ın tez çalışması Elektronik Mühendisliği Anabilim Dalında YÜKSEK LİSANS tezi olarak kabul edilmiştir.

JÜRİ

ÜYE
(TEZ DANIŞMANI) : Prof. Dr. Serkan Aksoy

ÜYE : Prof. Dr. Mansur İSGENDEROĞLU

ÜYE : Dr. Öğr. Üyesi Erkul BAŞARAN

ONAY

Gebze Teknik Üniversitesi Fen Bilimleri Enstitüsü Yönetim Kurulu'nun

...../...../..... tarih ve ...../..... sayılı kararı.

SUMMARY

In this thesis, detection performance of a pulse induction metal detector is investigated by using Maxwell's equations based Quasi-Static Finite-Difference Time-Domain (QS-FDTD) method in three dimensional Cartesian coordinates. Type of source is a rectangular pulse wave which is excited by a magnetic dipole antenna. A numerical problem space is terminated with a modified Mur Absorbing Boundary Condition. The QS-FDTD solution is validated with a canonical problem of frequency signature calculations of a conducting sphere located in a weakly lossy medium. Time signatures of a buried metallic and an air cube are calculated for different scenarios. Thus, fundamental knowledge is obtained for the detection and classification of the buried objects.

Key Words: Quasi-Static Finite-Difference Time-Domain (QS-FDTD), Pulse Induction Metal Detector, Detection and Identification.

ÖZET

Bu tezde, Maxwell denklemi tabanlı Kuvazi-Statik Zaman-Uzayı Sonlu-Farklar (KS-ZUSF) yöntemi ile üç boyutlu Kartezyen koordinatlarda darbe indüksiyonlu bir metal detektörünün tespit başarımı zaman uzayında incelenmiştir. Kaynak işareti olarak dikdörtgen darbe dalga fonksiyonu kullanılmıştır. Sayısal problem uzayı modifiye edilmiş Mur tipi Soğurucu Sınır Koşulu uygulanarak sonlandırılmıştır. Düşük kayıplı bir ortamdaki iletken bir kürenin frekans imzası hesaplanarak yöntemin doğruluğu gösterilmiştir. Küp şeklindeki gömülü metal ve hava boşluğu için zaman imzaları farklı senaryolar için hesaplanmıştır. Böylece, gömülü cisimlerin tespiti ve sınıflandırılması için temel bilgi elde edilmiştir.

Anahtar Kelimeler: Kuvazi-Statik Zaman-Uzayı Sonlu-Farklar (KS-ZUSF), Darbe İndüksiyonu Metal Detektörü, Tespit ve Teşhis.

ACKNOWLEDGEMENTS

Firstly, I would like to express my special thanks to my supervisor Prof. Dr. Serkan Aksoy for his priceless guidance and suggestions. Without his expertise it is not possible to complete this study.

I also would like to give my special thanks to my beloved parents for their limitless supports in my all lifetime.

TABLE of CONTENTS

LIST of ABBREVIATIONS and ACRONYMS

Abbreviations and Acronyms		**Explanations**
m	:	Meter
s	:	Second
V	:	Volt
A	:	Ampere
C	:	Coulomb
Wb	:	Weber
F	:	Farad
H	:	Henry
S	:	Siemens
Hz	:	Hertz
kHz	:	Kilohertz
∇	:	Nabla operator
j	:	Imaginary number ($\sqrt{-1}$)
$\vec{H}$	:	Magnetic field vector ($\mathrm{A/m}$)
$\vec{E}$	:	Electric field vector ($\mathrm{V/m}$)
$\vec{B}$	:	Magnetic flux density ($\mathrm{Wb/m^2}$)
$\vec{D}$	:	Displacement currents ($\mathrm{C/m^2}$)
$\vec{J}$	:	Current density ($\mathrm{A/m^2}$)
ρ	:	Charge density ($\mathrm{C/m^3}$)
ε	:	Dielectric permittivity ($\mathrm{F/m}$)
ε_0	:	Dielectric permittivity of free space ($\mathrm{F/m}$)
ε^{QS}	:	Scaled dielectric permittivity ($\mathrm{F/m}$)
μ	:	Magnetic permeability ($\mathrm{H/m}$)
μ_0	:	Magnetic permeability of free space ($\mathrm{H/m}$)
σ	:	Conductivity (S)
c	:	Velocity of light ($\mathrm{m/s}$)
ω	:	Angular frequency ($\mathrm{rad/s}$)

f	:	Frequency (Hz)
λ	:	Wavelength (m)
k	:	Wave number (rad/m)
k^N	:	Numerical wave number (rad/m)
Z	:	Wave impedance (Ohm)
δ	:	Skin depth
t	:	Time (s)
L_x	:	Length on the direction of x (m)
L_y	:	Length on the direction of y (m)
L_z	:	Length on the direction of z (m)
h	:	Height of the source (m)
d_c	:	Depth of the cube (m)
d_s	:	Depth of the soil (m)
N_x	:	Number of cells on the direction of x
N_y	:	Number of cells on the direction of y
N_z	:	Number of cells on the direction of z
Δx	:	Unit cell size on the direction of x (m)
Δy	:	Unit cell size on the direction of y (m)
Δz	:	Unit cell size on the direction of z (m)
n	:	Time step number
Δt	:	Unit time step (s)
Δt^{QS}	:	Scaled unit time step (s)
α	:	Quasi-Static scaling coefficient
τ_e	:	Relaxation time (s)
τ_t	:	Transmit time (s)
τ_m	:	Magnetic diffusion time (s)
I	:	In phase part of signal
Q	:	Quadrature part of signal
ABC	:	Absorbing Boundary Condition
CFL	:	Courant-Friedrichs-Levy
CN-FDTD	:	Crank-Nicolson Finite-Difference Time-Domain
CPU	:	Central Processing Unit
CW	:	Continuous Wave

EMI	:	Electromagnetic Induction
EMF	:	Electromotive Force
EQS	:	Electro-Quasi-Static
FD	:	Frequency Domain
FDFD	:	Finite-Difference Fourier-Domain
FDTD	:	Finite-Difference Time-Domain
FEM	:	Finite Element Method
FOMUR	:	First Order Mur
IBC	:	Impedance Boundary Conditions
MoM	:	Method of Moments
MPV	:	Man-Portable Vector
MQS	:	Magneto-Quasi-Static
NSMS	:	Normalized Surface Magnetic Source
ONVMS	:	Ortho-Normalize Volume Magnetic Source
OWWE	:	One Way Wave Equation
PI	:	Pulse Induction
PML	:	Perfectly Matched Layer
QS	:	Quasi-Static
QS-FDTD	:	Quasi-Static Finite-Difference Time-Domain
RMS	:	Root Mean Square
SEA	:	Spheroidal Excitation Approach
SNR	:	Signal to Noise Ratio
SOMUR	:	Second Order Mur
TD	:	Time Domain
TEM	:	Transient Electromagnetic
UXO	:	Unexploded Ordnance

LIST of FIGURES

LIST of TABLES

1. INTRODUCTION

1.1. Overview

Metal detectors are a kind of devices based on Electromagnetic Induction (EMI) principle at low frequencies from 100 Hz to 100 kHz. Their aim is to detect buried dangerous or valuable metallic objects. These devices can be used as fixed frames (installed e.g. at the airports) or portable forms. The portable detectors are generally used for humanitarian and military demining, archeological investigations and gold hunting.

The operational principle of a metal detector is depicted in Figure 1.1. A transmitter coil excites electromagnetic waves and induces Eddy currents in a metallic object. The Eddy currents give rise to a secondary electromagnetic radiation. This secondary field is measured by a receiver coil. Therefore, a detection process is completed.

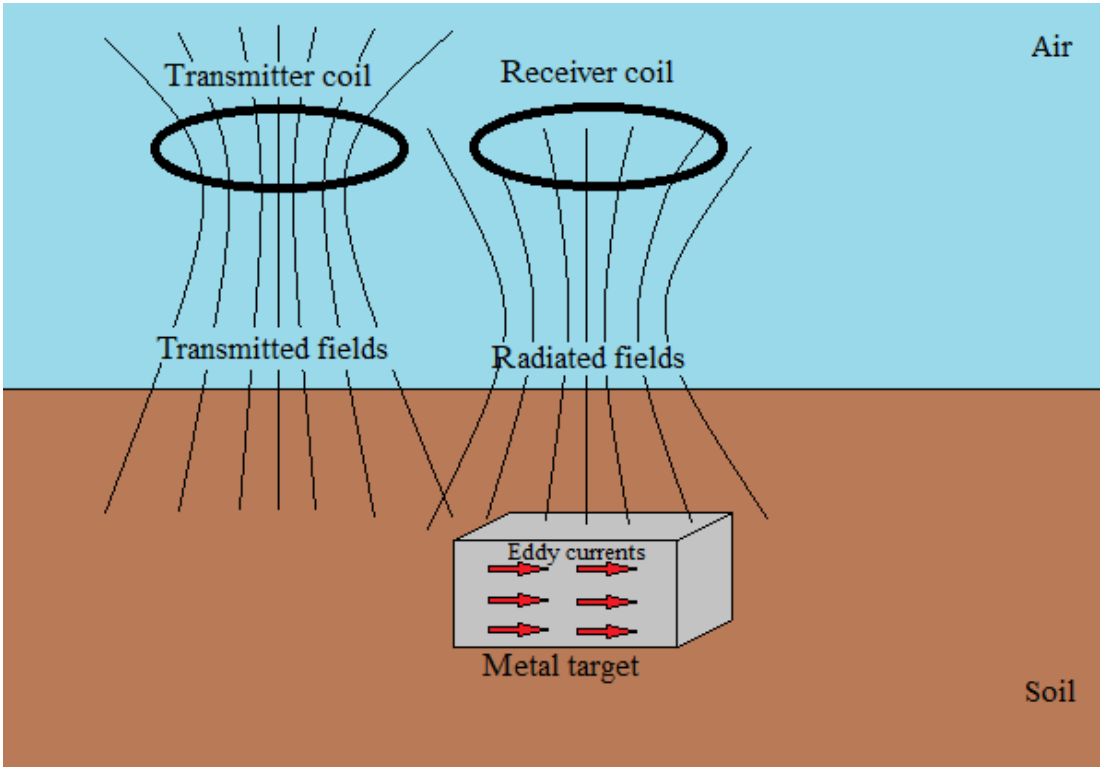

Figure 1.1: The operational principle of the metal detector.

There are two main metal detector types basing on their source signals. These are *Continuous Wave (CW)* and *Pulse Induction (PI)* metal detectors.

- The Continuous Wave (CW) metal detectors

The operational principle of the CW metal detectors is that a continuous sinusoidal signal at a single frequency or multiple frequencies is used as a transmitted signal. A secondary magnetic field originated from the metallic object is received. In general, analyses of the CW detectors are made in the frequency domain. Therefore, they are also named as Frequency Domain (FD) metal detectors.

- The Pulse Induction (PI) metal detectors

The principle of the PI metal detectors is that a pulse shaped signal is used as a transmitted signal. A secondary magnetic field from the metallic object is received. The PI detectors usually use rectangular pulses which have pulse lengths from 50μs to 500μs. An example for a source (primary) pulse current and the secondary induced voltage waveforms are shown in Figure 1.2. Analyses of the PI metal detectors are performed in the time domain. Therefore, they are also named as Time Domain (TD) metal detectors.

The one of the problem for the PI metal detectors is discrimination ability with strong background signals from difficult soils consist of magnetic particles. These particles can cause different time decay than the buried objects. On the other hand, one of the disadvantages of the PI metal detectors is susceptibility on the humidity and temperature. To overcome this problem is not easy and needs advanced research [Aksoy, 2018].

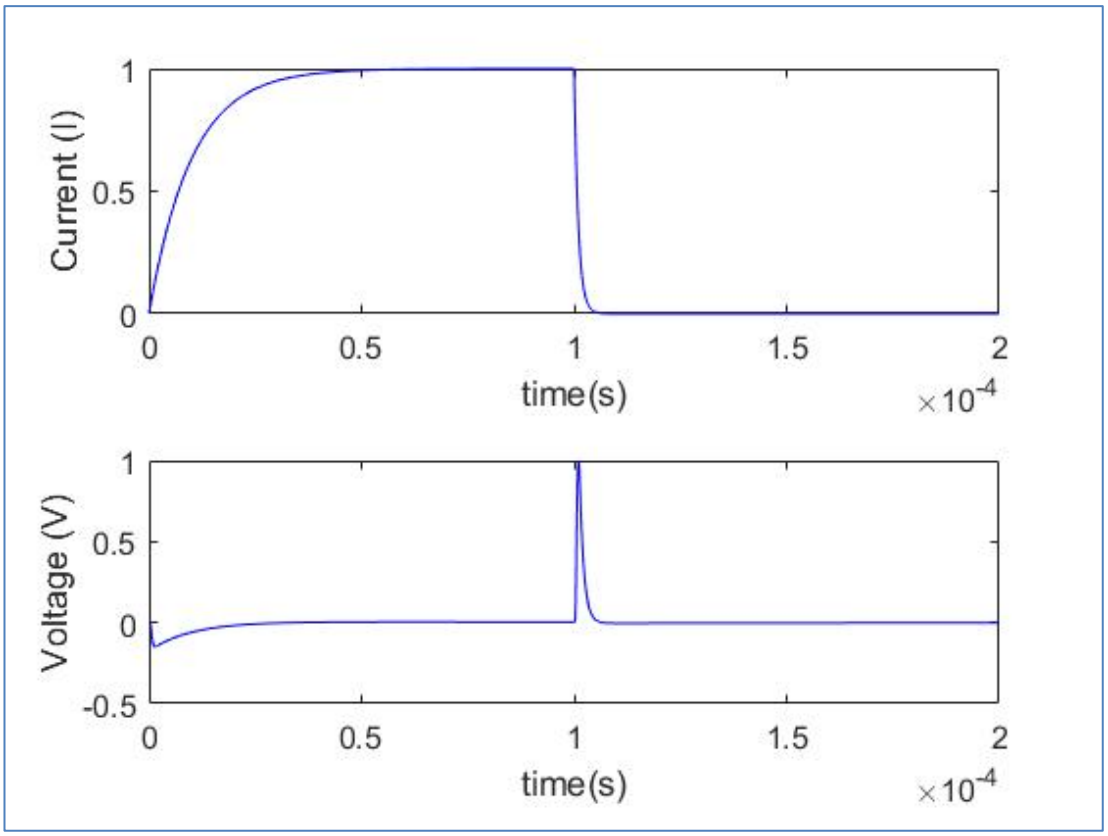

Figure 1.2: The source current waveform and received voltage response.

The rise-time of the secondary induced voltage is equal to the fall-time of the transmitted magnetic field since the Electromotive Force (EMF) causing the Eddy current, proportional to time derivative of the magnetic induction field strength. However, the fall time, that is the electrical time constant, depends on the shape, size and magnetic properties of the object. For poor conductors, the electrical time constant is small and for good conductors it is large. It is also bigger for large objects [Colani, 1966], [Colani and Aitken, 1966], [Jiracek, 2017].

The metal detectors can also be classified as *Monostatic* and *Bistatic* due to their configuration of the receiver and transmitter antennas. The monostatic systems are commonly used for the mine detection and gold hunting. In these systems, the receiver and transmitter are located as a concentric form, shown in Figure 1.3. In the PI detectors, the same coil can also be used as the transmitter and receiver antenna.

In the bistatic systems, the transmitter is fixed and the receiver is generally shifted horizontally as shown in Figure 1.4.

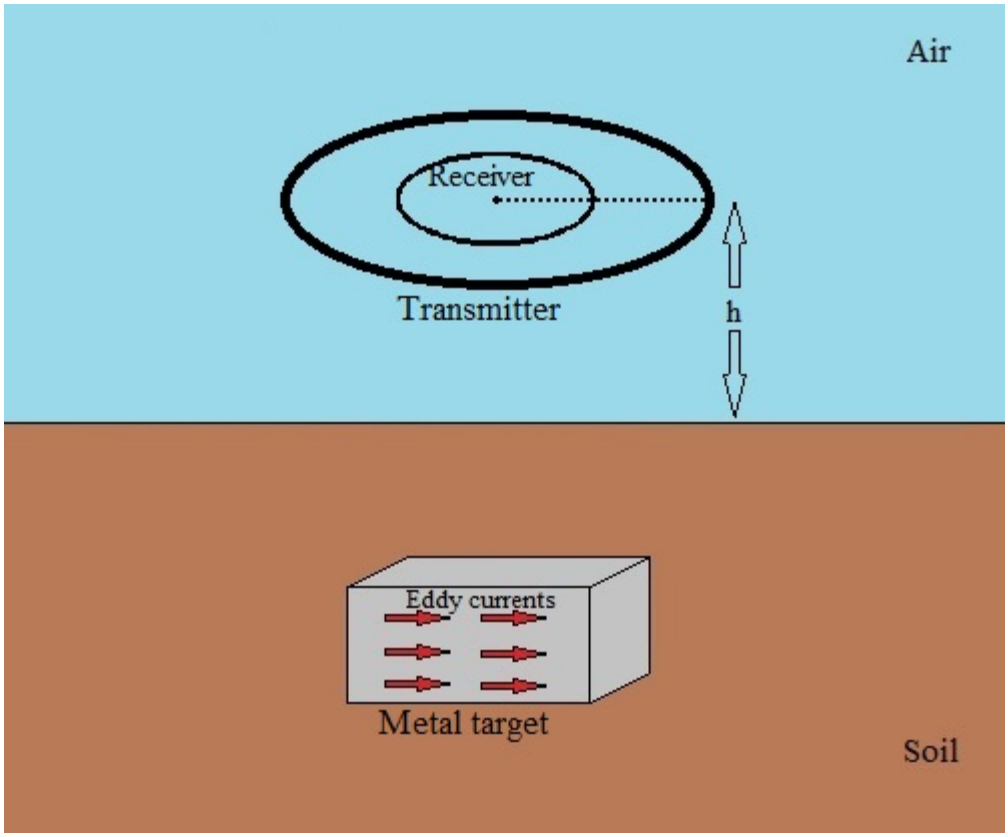

Figure 1.3: Monostatic antenna placements.

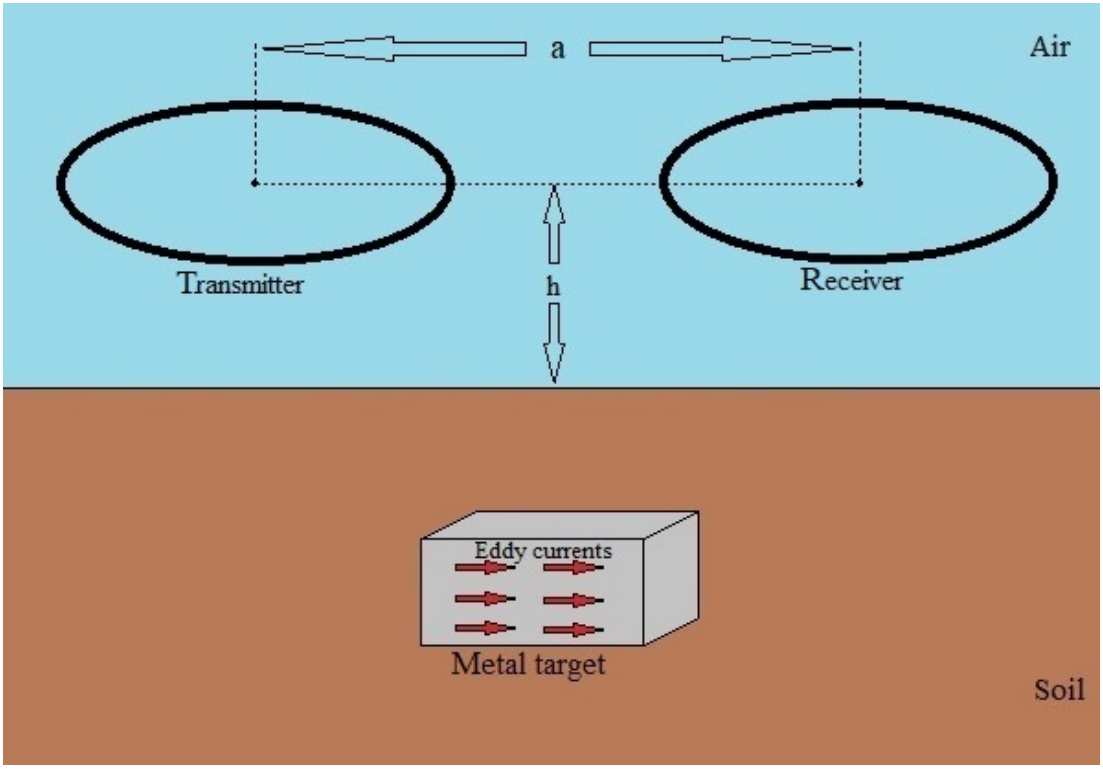

Figure 1.4: Bistatic antenna placement.

The PI detectors have some advantages;

- they can be designed with only single coil,
- the associated electronics is relatively simple,
- weak resistance to soil signals of small ferromagnetic particles,
- the instruments have low power consumption.

However, these instruments have limited capability to challenge the two most serious problems of modern metal detectors:

- strong background signal from magnetic soil and
- false alarms arising from different metal scraps.

In some cases, the CW detectors may be more suitable to suppress these problems (noises) with a narrow band filter [Ripka and Lewis, 2006], [Ripka et al., 2006].

1.2. Historical Development

In this section, the historical developments of the QS-FDTD method and PI metal detectors will be discussed, separately.

- Historical Developments of the QS-FDTD Method

In low frequency problems, it is not feasible to use classical Finite-Difference Time-Domain (FDTD) method because of extremely large wavelength corresponding to very long iteration times for a simulation of a full source period.

Consideration of the quasi-static approximation in the FDTD method is a solution to overcome to this problem. If the quasi-static criterion is valid, the classical FDTD method can be modified by slowing down the propagation velocity. In this manner, the FDTD unit time step can be extended efficiently for solution of the low frequency problems [Özakın and Aksoy, 2016].

Details of the FDTD and QS-FDTD method will be explained in Chapter 5.

- Historical Developments of the Pulse Induction Metal Detectors

The history of the PI metal detectors is a very wide topic. Therefore, it will be explained in Chapter 2, 3 and 4 in detail.

1.3. The Purpose and the Scope of this Thesis

In the literature, there are no sufficient, full and realistic analytical or numerical solutions for the PI metal detector. Therefore, behavior of the system is not well-understand. To eliminate lack of knowledge in this topic, the PI metal detector is simulated by using the QS-FDTD method in this thesis. Consequently, useful information for classification and discrimination purposes can also be obtained.

2. MODELING AND SIMULATION

2.1. Analytical Methods

2.1.1. Circuit Modeling

Riggs et al. developed an equivalent circuit model to calculate time domain response of a buried object excited by a transmitter dipole. A quadrupole antenna was used as a receiver. The calculations were made using the Laplace transform for a pulse and continuous wave excitation. The induced current in the receiver was calculated as a function of time. The frequency domain response was also calculated. In the circuit model, direct coupling between the transmitter and receiver was assumed to be zero. For the direct coupling, the experimental investigations were performed. The results showed that the direct coupling in the case of the symmetric receiver position was reduced -70 dB comparing to the arbitrary receiver positions [Riggs et al., 2002].

2.1.2. Helmholtz Equation

2.1.2.1. Laplace Transform Solution

Wait investigated a magnetic dipole (or a small current-carrying loop) propagation in an isotropic medium. The Laplace transform solution of the wave equation was used in the cylindrical coordinates. A Hertz (potential) vector was used for the formulation. At large values of the time, a static approximation was used. A rectangular pulse (step function current) response of the dipole in the sea water was calculated at the different distances of the observation point [Wait, 1953].

2.1.3. Diffusion Equation

Nabighian calculated transient response of a conducting permeable sphere excited by a magnetic dipole source in the free space using the solution of diffusion

equation. The dipole source solution was obtained from the differentiation of the pole source solution. Different orders of the multipoles were calculated for the different permeability values [Nabighian, 1970].

2.1.3.1. Inverse Fourier Transformation

2.1.3.1.1. Exact Solution

- Free Space and Conducting Half Space

Nabighian computed transient response of the earth due to an arbitrary loop located at the earth's surface using the Fourier transform solution of diffusion equation. A step function was used for the source excitation. The contour plots of the current density in the earth for the different moments were calculated [Nabighian, 1979].

Bowler and Johnson computed time domain response of a conducting half space excited by a coil of rectangular cross section using the inverse Laplace transform solution ($s = j\omega$) of diffusion equation. The coil was excited by a unit step function. The integrated EMF (Electro Motive Force) and field changes were calculated for the different time constants at the different heights of the coil. The analytical results were confirmed with the experimental results [Bowler and Johnson, 1997].

Karmis et al. calculated time domain response of a layered earth using the inverse Laplace transform ($s = j\omega$) solution of diffusion equation. Two concentric loops were used as a receiver and transmitter, both located on the surface of the earth. The transmitter coil was excited by a rectangular pulse. The induced voltages and effective resistivities as functions of time were calculated for the two, three, four and five layers earth models for the different thickness of layers, the different sizes of the coils and the different conductivity values of the some layers. The advantages of this method were pointed out comparing to the electrical DC method [Karmis et al., 2003].

Das calculated time domain response of conducting magnetic soil from a loop antenna excited by a step function. The time domain results were obtained from the inverse Laplace transform of the frequency domain solution of the diffusion

equation. A coplanar receiver and transmitter coils were located in the free space. The equivalent magnetic and electric dipole models were used for the solutions. The time signatures of the soils for the different conductivities and magnetic susceptibilities were calculated [Das, 2004].

2.1.3.1.2. Series Expansion

- Object in Free Space

Time domain EMI response of a conducting permeable sphere excited by a transmitter coil antenna with a pulse and pulse train signals (for non-homogeneous fields) was calculated by solving diffusion equation inside the sphere and Maxwell's equations outside the sphere. The time signatures for the different permeability values of the aluminum and steel spheres at the different depths were found by taking the inverse Laplace transform ($s = j\omega$) of the frequency domain solution. The analytical solutions were compared with the experimental results [Das et al, 1984].

Das et al. studied for determination of the depth of a shallowly buried conducting and permeable sphere by an induced voltage ratio of two receiver coils. The two receiver coils and one transmitter coil were located at the different heights above the earth in the free space. The transmitter coil was excited a by the periodic pulse train signal. For the time domain results, the inverse Laplace transform solution of the diffusion equation was used. The voltage ratios as functions of the time and depth were calculated for the different permeability and conductivity values of the sphere. The analytical results were verified with the experimental results. In conclusion, it was mentioned that the proposed method is not applicable for the different shaped materials [Das et al., 1985].

Song et al. calculated Transient Electromagnetic (TEM) response of a highly conducting and permeable cylinder using the inverse Fourier transform solution of diffusion equation with a model-based Spheroidal Excitation Approach (SEA) method. The frequency domain response and time signatures were calculated. The frequency domain results were validated with the measurements using the Geophex GEM-3 frequency domain EMI sensor; the time domain results were validated with the measurements using the Geonics EM 63 time domain EMI sensor. The different orientations of the cylinder were also analyzed [Song vd, 2008].

– Numerical Integration

Raiche and Spies calculated inverse Laplace transform solution of diffusion equation using a Gaussian quadrature numerical integration method for interpreting of apparent conductivity curves of two-layer earths using a transmitting loop antenna. The antennas were excited by a step function, half sine wave and sawtooth signal. The apparent conductivity curves were shown as functions of time [Raiche and Spies, 1981].

- Buried Objects in Lossy Medium

Wait calculated transient behavior of induced magnetic field of a conducting sphere in a relatively poorly conducting medium under a homogeneous magnetic field source. I/Q signature and time signature were extracted by solving the diffusion equation. Sinusoidal and step function sources were used for the frequency and time domain solutions, respectively. The inverse Fourier transform was used for the time domain results [Wait, 1951].

Wait and Spies investigated transient behavior of the induced magnetic fields in a conducting and permeable sphere located in a relatively poorly conducting medium with a homogeneous magnetic field excitation. Diffusion equation inside the sphere and Maxwell's equations outside the sphere were solved. The time domain results were obtained using the inverse Fourier transform. The impulse and step response of the non-permeable conducting sphere and, the step response of the permeable sphere with the different permeability values were calculated [Wait and Spies, 1969].

Wait and Ott calculated time domain impulse response of a non-magnetic conducting half-space from a magnetic dipole source using the inverse Laplace transform of the series expansion solution of diffusion equation in the cylindrical coordinates [Wait and Ott, 1972].

Singh calculated time domain response of a conducting sphere by a magnetic dipole source excited by a Heaviside function in a conducting infinite space. The analytical solution of the diffusion equation inside the sphere and the Laplace equation outside the sphere was utilized in the frequency domain at the spherical coordinates. The time domain responses were obtained for the different

conductivities and different orientations of the source. The inverse Fourier transform was used for the time domain calculations. Five independent functions were required for modeling the time domain response [Singh, 1973].

- Buried Objects in the Lossless Medium

Das calculated time domain response of a metallic sphere buried in non-conducting magnetically dispersive soil. A series expansion solution with the inverse Fourier transform used to solve the diffusion equation. Two concentric and coplanar circular coils used as a transmitter and receiver. The transmitter coil excited with a step function. The time signatures of the soil, aluminum sphere in the air and aluminum sphere in the soil at the different heights and different depths were calculated. The analytical results compared with the experiments using the Scheibel AN19/2 metal detector [Das, 2006].

2.1.3.2. Inverse Laplace Transformation

2.1.3.2.1. Exact Solution

- Free Space and Conducting Half Space

Bowler solved diffusion equation using the Laplace transform for the time domain response calculations of a conducting half space. A pancake shaped, a square section and a solenoid coil were used as a source. All these coils were excited by a unit step function. With the help of the reflection coefficient, the normalized coil EMF and its integrated response were calculated as a function of time [Bowler, 1990].

2.1.3.3. U-V Method

Davey and Han computed induced voltage in a conducting cylinder in the free space from the solution of a vector Helmholtz equation using U-V method that separates a vector equation into the two scalar equations. The inverse Laplace transform was used for the time domain data extraction. The time domain responses

for the different size of the cylinders and different time constants were obtained. The obtained results were also validated with the experimental results [Davey and Han, 1987].

2.2. Numerical Methods

2.2.1. Helmholtz Equation

2.2.1.1. Method of Moments

Sebak and Shafai calculated transient response of imperfectly conducting and permeable buried spheroidal objects excited by a circular transmitter loop antenna in the free space. Method of Moment (MoM) method was used with an Impedance Boundary Condition (IBC) in the frequency domain. The air-earth interface was neglected due to the high signal penetration into the soil. The inverse Fourier transform was used for the time domain data extraction. A periodic pulse train was used for a transmitter excitation. The time signatures were obtained for the different permeable materials at the different depths and orientations of the objects. The results were confirmed with an equivalent magnetic dipole method and analytical pulse induction technique [Sebak and Shafai, 1984].

2.2.1.2. Numerical Integral Calculation

Sebak et al. calculated transient response of rotationally symmetric permeable buried objects using a numerical solution (in frequency domain) of a magnetic field integral equation with the IBC. The air-earth interface was neglected due to the high signal penetration into the soil. The inverse Fourier transform was used for calculation of the time domain data. A circular loop antenna located in the free space was used as a transmitter and was excited by a periodic pulse train signal. The time signatures for the different permeability values and different orientations of the objects were calculated. The induced voltage as a function of position was also shown [Sebak et al., 1988].

2.2.2. Diffusion Equation

Mackie at al. solved diffusion equation using Finite Difference Fourier Domain (FDFD) method combined with an impedance matrix method. The magnetotelluric response of the layered earth was calculated at very low frequencies. A plane wave excitation was used as a source. Apparent resistivities were shown as functions of position and time for the different periods of the source. The results were compared with the integral equation solution [Mackie at al., 1993].

Uyeshima and Schultz computed electromagnetic induction response of an arbitrary heterogeneous conducting sphere by an external source placed in the air which is modeled with a very low conductivity. Three-dimensional FDFD method was used to solve the diffusion equation in the spherical coordinates. A minimum residual conjugate gradient method was used to solve the matrix system. The magnetic and electric field components were calculated as functions of geomagnetic co-latitude. The surface values of the magnetotelluric impedance and the magnetic field distributions were also shown. The results were compared with an integral equation solution and a quasi-analytical solution [Uyeshima and Schultz, 2000].

2.2.2.1. Crank-Nicholson (CN) FDTD

Chou et al. calculated time domain response of single, two and four layered conducting media under homogeneous fields using the 2D/3D Crank-Nicolson Finite-Difference Time-Domain (CN-FDTD) solution of diffusion equation with a conjugate gradient scheme. A periodic boundary condition was used. The numerical codes were speeded up with the CPU parallel programming. The time signatures for the different values of the conductivities were calculated with a sinusoidal and pulse excitation. The results were compared with the analytical solutions [Chou et al., 2000].

Hamano developed a three dimensional Crank-Nicolson Finite-Difference Time-Domain (CN-FDTD) algorithm to solve diffusion equation. Time domain response of a heterogeneous conducting sphere at very low frequencies was calculated. The impulse responses of the homogeneous earth and different model of the heterogeneous earths and the spatial distributions were calculated. The numerical

results were confirmed with the analytical results. In addition, the CN-FDTD method was compared with a staggered grid finite difference (in the frequency domain) method. The Fourier transform was used for the frequency domain transformation [Hamano, 2002].

Chou et al. developed a Crank-Nicholson FDTD algorithm to solve diffusion equation at the spherical coordinates. The magnetic field distribution of the layered earth was calculated with a magnetic dipole source excitation at very low frequencies. The numerical algorithm was speeded up with the CPU parallelization [Chou et al., 2001].

2.2.2.2. Finite Element Method (FEM)

Tsuboi et al. computed transient Eddy currents induced in an aluminum plate from an exciting coil using a time stepping method and a Fourier transform method. An axisymmetric Finite Element Method (FEM) was used with the coarse and fine meshing in the computation. Time dependency of the flux (with pulse and half sinusoidal excitations) and the time dependency of the Eddy current density were calculated for the 2-D and 3-D problems. The TEAM Workshop Problem 27 was analyzed for the 3-D transient Eddy current problem. The numerical results were compared with the analytical results [Tsuboi et al., 2004].

Ludwig and Dai computed transient response of a conducting and non-magnetic half space from an infinite wire and current loop antennas. The two dimensional weighted-residual-based FEM was used to solve the diffusion equation at the rectangular and cylindrical coordinates. A unit step function was used for the excitation. The spatial Eddy current distributions at the various time steps and the temporal Eddy currents at the various depths were computed. The field distributions with the subsurface defects were also shown. The numerical results were validated with the analytical models in the time domain employing the inverse Laplace transforms ($s = j\omega$) [Ludwig and Dai, 1990].

Dyck et al. performed a study for effect of a pulse shape on a signal amplitude for a round hole through a conducting (aluminum alloy) plate (TEAM Workshop Problem 27). The FEM method was used for the solution of the diffusion equation. The peak values for the different turn-off times and the time domain response of the

horizontal differential flux densities with the horizontal, square and vertical flaws were calculated. The peak differential flux density as a function of the width and height of the flaw was also shown. The analysis performed using MagNet transient analysis software from Infolytica Corporation. The numerical results were compared with the experimental results [Dyck et al., 2004].

Xie et al. developed a FEM (edge elements) algorithm based on a static solution combined with a linear interpolation method to detect a global wall thinning in the thick plates. The repetitive square waves were used for the excitation. The time domain solution was calculated by the Inverse Fourier transform. The differential magnetic fields as a function of time for the different number of harmonics and differential magnetic fields as a function of frequency for the different thicknesses of a plate were calculated. In order to compare the time domain results, the FEM time domain algorithm with a Crank-Nicholson time scheme was developed. The experiments were also performed for the same problem [Xie et al., 2011].

Antoun and Perriard developed a volumetric estimation method in the FEM simulation. This technique based on a modification of the finite element mesh of a target due to a magnetic vector potential variation in the two computational time steps. The computational times as a function of frequency for the seven different skin modeling cases were extracted. The results showed that the computational time can be reduced tenfold. An instantaneous vector potential derivative of a copper sphere, instantaneous Eddy current distribution of the steel and copper spheres and flux densities at the surface of the spheres of the different materials were computed. The joule heating as functions of time were also computed for the spheres, made of different materials. The numerical results were validated with the experiments [Antoun and Perriard, 2013].

3. IDENTIFICATION AND DISCRIMINATION

3.1. Simple Time Signatures

Chilaka et al. investigated detection performance of the Continuous Wave (CW) and Pulse Induction (PI) metal detectors using an equivalent circuit model and FEM solutions. The transmitted pulse duration of the PI detector was 800 µs with a 50 Hz (20 ms period) repetition frequency. The importance of the late time information was highlighted for better discrimination. The frequency band of the CW detector was extended down from 30 Hz – 24 kHz to 1 Hz – 24 kHz for the better discrimination performance. The CW detector performance was shown as a function of the Signal-to-Noise Ratio (SNR). The I/Q and time signatures of the copper loop were measured on the receiver. The results were compared with the circuit model solutions and FEM solutions. As the receiver, a shape-8 coil was used to compensate the noise effects. The I/Q and time signatures of the steel cylinders also were measured with the different wall thicknesses [Chilaka et al., 2005].

McFee et al. designed an EMI sensor system for measuring the time domain response of the conductive spheroidal objects in the free space. The sensor was comprised of the coaxial transmitter and receiver coils and the transmitter excited by the periodic pulse train signal. The time signatures for the different depth, electromagnetic properties, size, shape and orientation of the spheroidal objects were measured. The background noise information was also given [McFee et al., 1984].

3.2. Magnetic Polarizability Tensor

3.2.1. Object in Free Space

Ambruš et al. dealt with a problem of estimation time dependent directional magnetic polarizabilities using a planar time domain EMI sensor. The sensor consists of the three coaxial circular loops (the main transmitter, the bucking transmitter and receiver). The induced voltage distributions for the steel sphere, the steel cylinder and the aluminum cylinder were measured. The mean values of the magnetic

polarizabilities and their standard deviations were calculated for the same targets [Ambruš et al., 2016].

3.3. Dipole Model

3.3.1. Simple Dipole Model

3.3.1.1. Object in Free Space

Fernandez et al. designed a Man-Portable Vector (MPV) EMI sensor for classification of UXO like metallic objects based on a tensor dipole model. The EMI sensor consists of the five cubic receiver coils and one transmitter coil surrounds them. The device works at the two modes of the operation that the static mode (yields the higher SNR and lower data diversity) and the dynamic mode (yields the lower SNR and higher data diversity). The time domain responses at the different measurement points and the field distributions were measured. The polarizabilities as functions of time were also measured for the different scenarios: the different orientations of the objects, the different depths of the aluminum and steel cylinders, two UXOs and the one UXO with the nails [Fernandez et al., 2011].

Fernandez et al. designed a new version of the MPV EMI sensor named as a MPV-II. The MPV-II was used for the classification of the UXOs from the time domain data using a simple dipole model. The transverse and axial polarizability elements in the time domain were extracted from the one target, the one target with clutters and two targets scenarios for the various projectiles [Fernandez et al., 2011].

3.3.2. Advanced Dipole Model

3.3.2.1. Object in Free Space

Barrowes et al. developed a classification technique based on an advanced dipole model, Normalized Surface Magnetic Source (NSMS), using time domain data from the MPV EMI sensor. In this manner, the time signatures for the different

orientations and different depths of the various objects were analyzed with and without the noise effect [Barrowes et al., 2009].

Shubitidze et al. developed a high power EMI sensor for detection and classification of deeply buried metal objects. The sensor system consists of the four coplanar square transmitter loops and four tri-axial (cube) receiver coils placed at the center of each transmitter. The transmitter current is boosted from 6 A (previous version of the sensor) to 14 A. The Ortho-Normalized Volume Magnetic Source (ONVMS) model which is based on the distributed equivalent magnetic dipoles was used for the classification. For simplicity, the soil response was neglected. The total ONVMS data as a function of time for the different sizes of the UXOs were measured and the probability of detection was extracted [Shubitidze et al., 2016].

Shubitidze et al. studied for identification and classification of metallic objects using the time domain EMI sensor. The orthonormalized volume magnetic source (distributed magnetic dipoles) model was used for the identification. All the displacement currents were neglected for simplicity. A TEMTADS sensor array (5x5 grid of the concentric rectangular Tx-Rx antennas) was used for the measurements. The time decay curves for the single and multiple targets (the UXO, the aluminum and steel spheres and the spheroids) were extracted using the single and multiple sources [Shubitidze et al., 2014].

4. OTHER WORKS

4.1. Compensation

Nelson and Arabian developed a portable robot system for the PI metal detectors. The two concentric receiver-transmitter loops were placed on the robot symmetrically to compensate the influence of the electronic components of the system. The induced voltages in the number of calibration loops and coke can at a depth of 15 cm were measured [Nelson and Arabian, 2002].

Olhoeft and Strangway investigated effect of magnetic losses on the frequency signature (I/Q signature) of a permeable sphere with a Cole-Cole frequency distribution model. The series expansion solution of the diffusion equation was used for the calculation of the I/Q signatures. The magneto-electric and nonlinear effects were neglected. The I/Q signatures of the spheres with the constant permeabilities and different electrical time constants and the I/Q signatures of the sphere with the Cole-Cole frequency distribution model of the complex permeability with the different magnetic time constants were calculated. It was observed that the permeable materials change sign of the in-phase and quadrature components of the I/Q signatures at the frequencies higher than the peak electrical loss. The loss tangent spectrums for the different magnetic materials and the time decay curves of the copper and magnetite were also extracted. Therefore, it was noted that the complex permeability gives rise to the phase difference between the electrical and magnetic relaxation times. The analytical results were compared with the experimental results [Olhoeft and Strangway, 1974].

4.2. Conducting Half-Space (Earth)

4.2.1. Layered, Stratified

Mogilatov et al. calculated time domain response of a conducting half-space with an insulating layer using the inverse Laplace transform solution of Maxwell's equation. The electric and magnetic dipoles were used as the sources and excited by

a step function. The time domain electric field responses were obtained for the different permittivity values of the earth. It was shown that the insulating layer totally masks underlying resistivities with the quasi-static approximation [Mogilatov et al., 2014].

Verma and Mallick calculated transient response of three-layer earth by a coplanar loop system and loop wire element. The time domain data was obtained with the Fourier series summation technique. The transmitter antenna was excited by the half-sinusoidal and square pulses of the alternating polarity. The time domain responses of the three-layer earth were calculated for the different thickness ratios of the layers and the RMS difference were calculated as a function of thickness ratio. The frequency response was also calculated [Verma and Mallick, 1979].

4.3. Reports

Kim et al. proposed a magnetic sheet backing of a search coil to improve detection range of the PI detector which has a planar square spiral mono coil search coil. The magnetic field strength as a function of distance was simulated using ANSYS Maxwell Software for different thicknesses of the magnetic sheet. It was shown that with magnetic sheet, the field pattern stronger in one direction. The coil inductance and resistance were measured for different thicknesses of the magnetic sheet. It was observed that the inductance was increased while the resistance was not affected by the magnetic sheet. The time signatures were measured with and without the target (M15 anti-tank mine) and with and without the magnetic sheet. The rectangular pulse signal with 700 us pulse width and 1 kHz repetition frequency was used for the coil excitation. The detection range was also measured for the different thicknesses of the magnetic sheet and it was proven that the detection range was increased with the magnetic sheet. Furthermore, it was also noted that the weight of the sensor is heavy with the magnetic sheet. Therefore, it is more suitable for the vehicle mounted operations than the hand held operations [Kim et al, 2014].

5. FINITE-DIFFERENCE TIME-DOMAIN METHOD

Finite-Difference Time-Domain (FDTD) method is based on numerical calculation of spatial and temporal derivatives in Maxwell's equations via central, backward and forward differences approximation technique [Yee, 1966]. Mostly, central differences technique is preferred due to its higher accuracy. In the FDTD method, the numerical derivatives are replaced by Taylor series expansion with second or higher order accuracy. One of the major disadvantages of the FDTD method is the requirement of excessive temporal discrimination [Aksoy, 2017].

Some advantages of the FDTD method:

- *Does not use linear algebra*: Does not need matrix inversions. Theoretically, it has no limitation for number of unknowns.
- *Presents controllable numerical results*: Since it is well understood, the numerical solutions are under control.
- *Gives pulse response directly*: With a single run, it gives wide bandwidth pulse or sinusoidal steady state response.
- *Solves wide variety of problems due to geometry and material types*: It can be examined lossy, inhomogeneous, anisotropic, dispersive and nonlinear materials of complex geometries.
- *Presents full-wave solution*: It involves diffractions.
- *Real-time visualization is possible*: Electromagnetic field distributions can be viewed, instantaneously.

5.1. One Dimensional Finite Differences

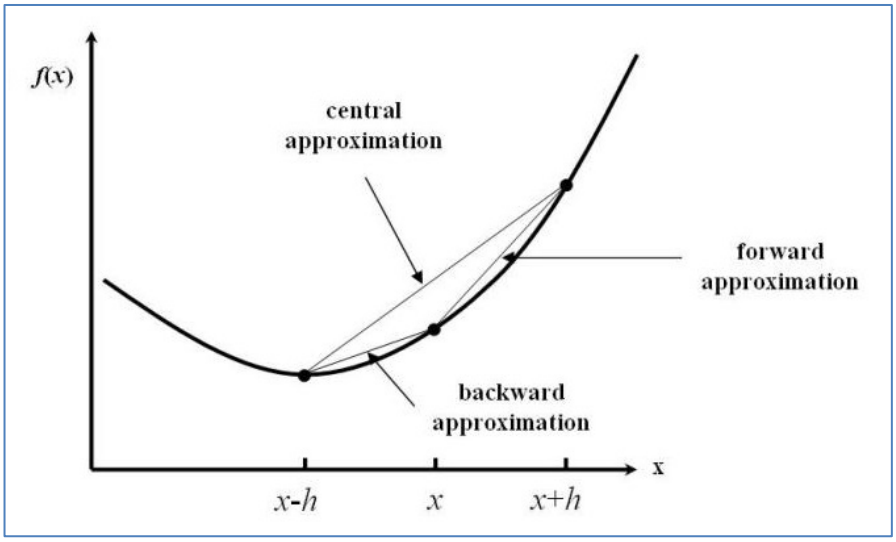

Figure 5.1: Types of the finite difference techniques.

One of the favorable numerical methods to solve differential equations is the finite differences technique. There are three different finite differences technique which are the forward, the backward and central differences as seen in Figure 5.1. To apply this technique to a differentiable function, the function should be discretized, initially. Therefore, a one dimensional $f(x)$ function is split by Δx unit cell size and number of i pieces. Then, the function can be shown below

$$x_i = i\Delta x \;\Rightarrow\; f(x) = f(x_i) = f(i\Delta x). \tag{5.1}$$

According to this, to obtain the derivative of $df(x)/dx$, Taylor series expansion of $f(x)$ is required at the point of $x = x_i$ as

$$\begin{aligned} f(x) = \sum_{n=0}^{\infty} \frac{f^n(x_i)}{n!}(x - x_i)^n \\ = f(x)|_{x=x_i} + (x - x_i)f'(x)|_{x=x_i} \\ + \frac{(x - x_i)^2}{2!} f''(x)|_{x=x_i} + \cdots \end{aligned} \tag{5.2}$$

If $h = (x - x_i)$, it can be written like below

$$f(x_i + h) = f(x_i) + hf'(x_i) + \frac{h^2}{2!}f''(x_i) + \cdots \tag{5.3}$$

Then, at $x = x_i$, the equation becomes

$$f(x + h) = f(x) + hf'(x) + \frac{h^2}{2!}f''(x) + \frac{h^3}{3!}f'''(x) + \cdots \tag{5.4}$$

then, it is found that

$$\frac{f(x + h) - f(x)}{h} = f'(x) + \frac{h}{2!}f''(x) + \frac{h^2}{3!}f'''(x) + \cdots \tag{5.5}$$

In a similar way for $f(x - h)$

$$f(x - h) = f(x) - hf'(x) + \frac{h^2}{2!}f''(x) - \frac{h^3}{3!}f'''(x) + \cdots \tag{5.6}$$

and

$$-\frac{f(x - h) - f(x)}{h} = f'(x) - \frac{h}{2!}f''(x) + \frac{h^2}{3!}f'''(x) - \cdots \tag{5.7}$$

then, summing these two equations, the central difference expression is found as

$$\frac{f(x + h) - f(x - h)}{2h} = f'(x) + \frac{h^2}{3!}f'''(x) + \cdots \tag{5.8}$$

Therefore, with the second order error $O(h^2)$, the first derivative of $f(x)$ becomes

$$f'(x) = \frac{f(x + h) - f(x - h)}{2h} + O(h^2). \tag{5.9}$$

In this manner, $df(x)/dx$ can be expressed using the central difference approximation with second order accuracy as

$$\frac{df(x)}{dx} \cong \frac{f(x+h) - f(x-h)}{2h}. \tag{5.10}$$

5.2. Finite Difference Time Domain Method and Maxwell's Equations

Spatial and temporal derivatives of Maxwell's equation are solved iteratively in the time domain using the finite difference technique. Maxwell's equations with space $(\vec{r})$ and time (t) dependencies is given

$$\begin{aligned} \nabla \times \vec{E}(\vec{r},t) &= -\frac{\partial}{\partial t}\vec{B}(\vec{r},t) \\ \nabla \times \vec{H}(\vec{r},t) &= \frac{\partial}{\partial t}\vec{D}(\vec{r},t) + \vec{J}(\vec{r},t) \\ \nabla \cdot \vec{D}(\vec{r},t) &= \rho(\vec{r},t) \\ \nabla \cdot \vec{B}(\vec{r},t) &= 0 \end{aligned} \tag{5.11}$$

where ∇ is Nabla operator, $\vec{E}(\vec{r},t)$ [V/m] , $\vec{B}(\vec{r},t)$ [Wb/m^2] , $\vec{H}(\vec{r},t)$ [A/m] , $\vec{D}(\vec{r},t)$ [C/m^2] , $\vec{J}(\vec{r},t)$ [A/m^2] and $\rho(\vec{r},t)$ [C/m^3] are electric field strength, magnetic induction field, magnetic field strength, displacement field, current density vector and charge density, respectively.

Firstly, let us apply the central differences to the time derivatives in the first Maxwell's equation. For Δt unit time step interval, the central difference expression of the first Maxwell's equation in $n\Delta t$ instant becomes

$$\nabla \times \vec{E}(\vec{r})\Big|^n \cong -\frac{\vec{B}(\vec{r})\Big|^{n+\frac{1}{2}} - \vec{B}(\vec{r})\Big|^{n-\frac{1}{2}}}{\Delta t} \tag{5.12}$$

where n is integer. For the latest term in time domain $\vec{B}(\vec{r})\Big|^{n+\frac{1}{2}}$, the update equation is obtained as follows

$$\vec{B}(\vec{r})\Big|^{n+\frac{1}{2}} \cong \vec{B}(\vec{r})\Big|^{n-\frac{1}{2}} - \Delta t\left[\nabla \times \vec{E}(\vec{r})\Big|^n\right]. \tag{5.13}$$

Similarly, for the second Maxwell's equation, if the central difference is taken for time derivatives at $(n+1/2)\Delta t$ moment, the update equation for $\vec{D}(\vec{r})\Big|^{n+1}$ is found as below

$$\vec{D}(\vec{r})\Big|^{n+1} \cong \vec{D}(\vec{r})\Big|^{n} - \Delta t\left[\vec{J}(\vec{r})\Big|^{n+\frac{1}{2}} - \nabla \times \vec{H}(\vec{r})\Big|^{n+\frac{1}{2}}\right]. \tag{5.14}$$

As it turns out, the electric and magnetic fields are shifted in the time and space relatively to each other. To apply the FDTD method to Maxwell's equations, only first two Maxwell's equations will be enough because, the last two equations are inherently provided by placements of the electric and magnetic fields in the FDTD cell [Taflove, 2005].

5.3. FDTD Update Equations with Loss in Cartesian Coordinates

Maxwell's equations in a simple lossy medium are

$$\begin{aligned} \nabla \times \vec{E}(\vec{r},t) &= \mu \frac{\partial}{\partial t}\vec{H}(\vec{r},t) \\ \nabla \times \vec{H}(\vec{r},t) &= \varepsilon \frac{\partial}{\partial t}\vec{E}(\vec{r},t) + \sigma\vec{E}(\vec{r},t) + \vec{J}(\vec{r},t) \end{aligned} \tag{5.15}$$

where ε [F/m], μ [H/m] and σ [S/m] are permittivity, permeability and conductivity of the medium, respectively. In the Cartesian coordinates, each field components become

$$\begin{aligned} \frac{\partial H_x}{\partial t} &= \frac{1}{\mu}\left(\frac{\partial E_y}{\partial z} - \frac{\partial E_z}{\partial y}\right) & \frac{\partial E_x}{\partial t} &= \frac{1}{\varepsilon}\left(\frac{\partial H_z}{\partial y} - \frac{\partial H_y}{\partial z} - \sigma E_x - J_x\right) \\ \frac{\partial H_y}{\partial t} &= \frac{1}{\mu}\left(\frac{\partial E_z}{\partial x} - \frac{\partial E_x}{\partial z}\right) & \frac{\partial E_y}{\partial t} &= \frac{1}{\varepsilon}\left(\frac{\partial H_x}{\partial z} - \frac{\partial H_z}{\partial x} - \sigma E_y - J_y\right) \\ \frac{\partial H_z}{\partial t} &= \frac{1}{\mu}\left(\frac{\partial E_x}{\partial y} - \frac{\partial E_y}{\partial x}\right) & \frac{\partial E_z}{\partial t} &= \frac{1}{\varepsilon}\left(\frac{\partial H_y}{\partial x} - \frac{\partial H_x}{\partial y} - \sigma E_z - J_z\right). \end{aligned} \tag{5.16}$$

These field components are discretized in the space and time and located in the FDTD unit cell as shown in Figure 5.2. The cell locations are expressed with (i, j, k) terms along (x, y, z) directions, respectively. The spatial and temporal discretization of the electric and magnetic field components are shifted relative to each other. In the time discretization, the magnetic and electric field components are placed on the integer and half values of the time steps, respectively.

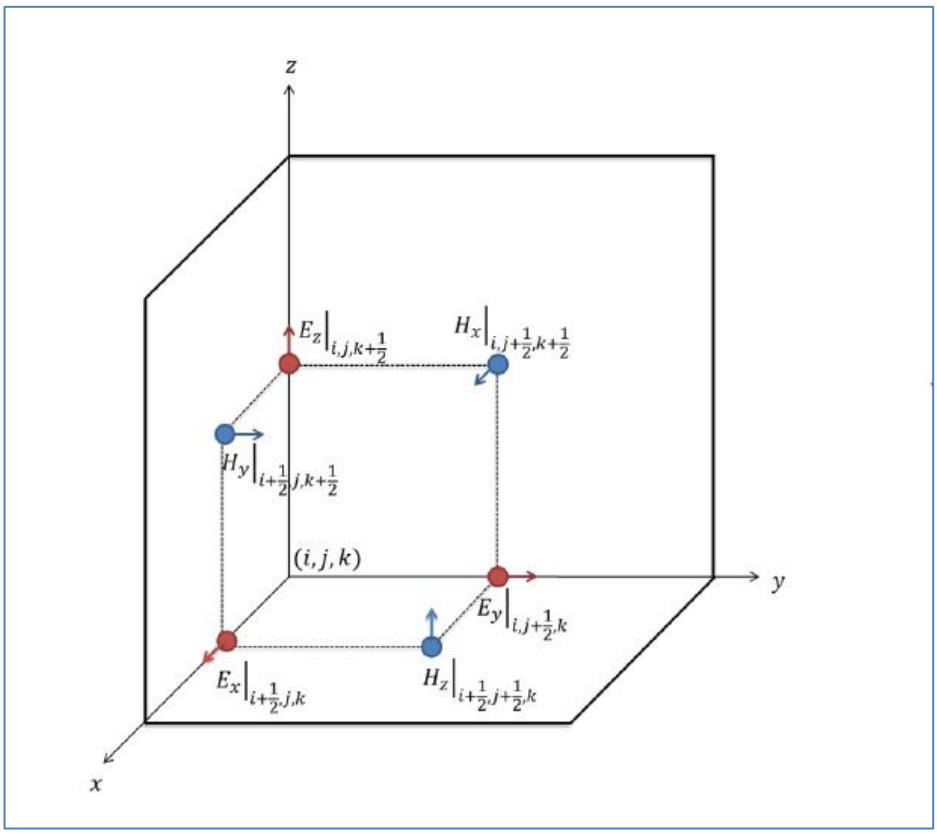

Figure 5.2: The field components in the unit Yee cell.

If the temporal and spatial derivatives are expressed with the central differences, the update equations of each magnetic field components are obtained as

$$H_x\big|_{i,j+\frac{1}{2},k+\frac{1}{2}}^{n+\frac{1}{2}} = H_x\big|_{i,j+\frac{1}{2},k+\frac{1}{2}}^{n-\frac{1}{2}} + \frac{\Delta t}{\mu_{i,j+\frac{1}{2},k+\frac{1}{2}}}\left[-\frac{E_z\big|_{i,j+1,k+\frac{1}{2}}^{n} - E_z\big|_{i,j,k+\frac{1}{2}}^{n}}{\Delta y} + \frac{E_y\big|_{i,j+\frac{1}{2},k+1}^{n} - E_y\big|_{i,j+\frac{1}{2},k}^{n}}{\Delta z}\right] \tag{5.17}$$

$$H_y\big|_{i+\frac{1}{2},j,k+\frac{1}{2}}^{n+\frac{1}{2}} = H_y\big|_{i+\frac{1}{2},j,k+\frac{1}{2}}^{n-\frac{1}{2}} + \frac{\Delta t}{\mu_{i+\frac{1}{2},j,k+\frac{1}{2}}}\left[-\frac{E_z\big|_{i+1,j,k+\frac{1}{2}}^{n} - E_z\big|_{i,j,k+\frac{1}{2}}^{n}}{\Delta x} + \frac{E_x\big|_{i+\frac{1}{2},j,k+1}^{n} - E_x\big|_{i+\frac{1}{2},j,k}^{n}}{\Delta z}\right] \tag{5.18}$$

$$H_z\big|_{i+\frac{1}{2},j+\frac{1}{2},k}^{n+\frac{1}{2}} = H_z\big|_{i+\frac{1}{2},j+\frac{1}{2},k}^{n-\frac{1}{2}} + \frac{\Delta t}{\mu_{i+\frac{1}{2},j+\frac{1}{2},k}}\left[-\frac{E_x\big|_{i+\frac{1}{2},j+1,k}^{n} - E_x\big|_{i+\frac{1}{2},j,k}^{n}}{\Delta y} + \frac{E_y\big|_{i+1,j+\frac{1}{2},k}^{n} - E_y\big|_{i,j+\frac{1}{2},k}^{n}}{\Delta x}\right]. \tag{5.19}$$

Because of the half time step is not defined in the FDTD algorithm, the mean value of two time steps is used for the electric field components like below

$$E_x\big|_{i+\frac{1}{2},j,k}^{n+\frac{1}{2}} = \frac{E_x\big|_{i+\frac{1}{2},j,k}^{n+1} + E_x\big|_{i+\frac{1}{2},j,k}^{n}}{2} \tag{5.20}$$

and the update equations for the each electric field components are obtained as

$$E_x\big|_{i+\frac{1}{2},j,k}^{n+1} = \left(\frac{2\varepsilon_{i+\frac{1}{2},j,k} - \Delta t\sigma_{i+\frac{1}{2},j,k}}{2\varepsilon_{i+\frac{1}{2},j,k} + \Delta t\sigma_{i+\frac{1}{2},j,k}}\right) E_x\big|_{i+\frac{1}{2},j,k}^{n} + \left(\frac{2\Delta t}{2\varepsilon_{i+\frac{1}{2},j,k} + \Delta t\sigma_{i+\frac{1}{2},j,k}}\right)\left[\frac{H_z\big|_{i+\frac{1}{2},j+\frac{1}{2},k}^{n+\frac{1}{2}} - H_z\big|_{i+\frac{1}{2},j-\frac{1}{2},k}^{n+\frac{1}{2}}}{\Delta y} - \frac{H_y\big|_{i+\frac{1}{2},j,k+\frac{1}{2}}^{n+\frac{1}{2}} - H_y\big|_{i+\frac{1}{2},j,k-\frac{1}{2}}^{n+\frac{1}{2}}}{\Delta z} - J_x\big|_{i+\frac{1}{2},j,k}^{n+\frac{1}{2}}\right] \tag{5.21}$$

$$E_y\big|_{i,j+\frac{1}{2},k}^{n+1} = \left(\frac{2\varepsilon_{i,j+\frac{1}{2},k} - \Delta t\sigma_{i,j+\frac{1}{2},k}}{2\varepsilon_{i,j+\frac{1}{2},k} + \Delta t\sigma_{i,j+\frac{1}{2},k}}\right) E_y\big|_{i,j+\frac{1}{2},k}^{n} + \left(\frac{2\Delta t}{2\varepsilon_{i,j+\frac{1}{2},k} + \Delta t\sigma_{i,j+\frac{1}{2},k}}\right)\left[\frac{H_x\big|_{i,j+\frac{1}{2},k+\frac{1}{2}}^{n+\frac{1}{2}} - H_x\big|_{i,j+\frac{1}{2},k-\frac{1}{2}}^{n+\frac{1}{2}}}{\Delta z} - \frac{H_z\big|_{i+\frac{1}{2},j+\frac{1}{2},k}^{n+\frac{1}{2}} - H_z\big|_{i-\frac{1}{2},j+\frac{1}{2},k}^{n+\frac{1}{2}}}{\Delta x} - J_y\big|_{i,j+\frac{1}{2},k}^{n+\frac{1}{2}}\right] \tag{5.22}$$

$$E_z\big|_{i,j,k+\frac{1}{2}}^{n+1} = \left(\frac{2\varepsilon_{i,j,k+\frac{1}{2}} - \Delta t\sigma_{i,j,k+\frac{1}{2}}}{2\varepsilon_{i,j,k+\frac{1}{2}} + \Delta t\sigma_{i,j,k+\frac{1}{2}}}\right) E_z\big|_{i,j,k+\frac{1}{2}}^{n} + \left(\frac{2\Delta t}{2\varepsilon_{i,j,k+\frac{1}{2}} + \Delta t\sigma_{i,j,k+\frac{1}{2}}}\right)\left[\frac{H_y\big|_{i+\frac{1}{2},j,k+\frac{1}{2}}^{n+\frac{1}{2}} - H_y\big|_{i-\frac{1}{2},j,k+\frac{1}{2}}^{n+\frac{1}{2}}}{\Delta x} - \frac{H_x\big|_{i,j+\frac{1}{2},k+\frac{1}{2}}^{n+\frac{1}{2}} - H_x\big|_{i,j-\frac{1}{2},k+\frac{1}{2}}^{n+\frac{1}{2}}}{\Delta y} - J_z\big|_{i,j,k+\frac{1}{2}}^{n+\frac{1}{2}}\right]. \tag{5.23}$$

5.4. Numerical Dispersion

Dispersion is a phenomenon that phase velocity of the electromagnetic wave will depend on frequency. On the other hand, numerical dispersion is a dispersion caused by FDTD meshing. In this manner, the numerical dispersion can cause some undesired situations:

- Non-physical results,
- Insufficient accuracy for phase canceling in multiple scatterings,
- Numerical anisotropy,
- Fake refractions.

Numerical dispersion depends on

- Wavelength,
- Direction of wave propagation in mesh,
- Sort of mesh and discretization.

The numerical dispersion relation for the three dimensional FDTD in the Cartesian coordinates is given

$$\left[\frac{1}{c\Delta t}\sin\left(\frac{\omega\Delta t}{2}\right)\right]^2 = \left[\frac{1}{\Delta x}\sin\left(\frac{k_x^N\Delta x}{2}\right)\right]^2 + \left[\frac{1}{\Delta y}\sin\left(\frac{k_y^N\Delta y}{2}\right)\right]^2 + \left[\frac{1}{\Delta z}\sin\left(\frac{k_z^N\Delta z}{2}\right)\right]^2 \tag{5.24}$$

where k_x^N, k_y^N and k_z^N show the numerical wavelength on the directions of x, y and z, respectively. When $k^2 = (k_x^N)^2 + (k_x^N)^2 + (k_x^N)^2$, a dispersionless situation is ensured where $k = \omega/c$ is an analytical wavenumber. Therefore, to decrease the numerical dispersion error, Δx, Δy and Δz should be chosen minimum as much as

possible. Mostly, it is sufficient to choose the cell size nearby $\lambda/10$ [Taflove and Hagness, 2005].

5.5. Numerical Stability

All numerical solutions must be stable. Therefore, to maintain the stability in the sense of the spatial and temporal discretization, the FDTD method must satisfy Courant-Friedrichs-Lewy (CFL) stability condition. Within this scope, for the numerical stability of the FDTD method in the three dimensional Cartesian coordinates, the unit time step must satisfy the following condition

$$\Delta t \leq \frac{1}{c\sqrt{\frac{1}{\Delta x^2}+\frac{1}{\Delta y^2}+\frac{1}{\Delta z^2}}} \tag{5.25}$$

where c is velocity of the light [Chu et al., 1991].

5.6. Mur Absorbing Boundary Condition

Many applications of the FDTD method are generally open space problems. However, the FDTD method must work in the finite spaces. To model the open space problems with the FDTD method, the finite space must be terminated with no reflecting boundaries. This boundary condition is named as *Absorbing Boundary Condition, ABC*. There are many ABC types in the FDTD applications. From these techniques, Perfectly Matched Layer (PML) has highest accuracy but it is hard for programming and it has heavy computation burden. In this work, a modified second order Mur type ABC is used because of its simplicity for programming.

5.6.1. One-Way Enquist-Majda Wave Equation

One-Way Wave Equation (OWWE) models wave propagation along one direction. If the OWWE is analytically applied to the any boundaries, there is no

reflection. In the Cartesian coordinates, the three dimensional wave equation in an operator form is

$$\begin{aligned}\frac{\partial^2}{\partial x^2}u(x,y,z,t)+\frac{\partial^2}{\partial y^2}u(x,y,z,t)+\frac{\partial^2}{\partial z^2}u(x,y,z,t)\\ -\frac{1}{c^2}\frac{\partial^2}{\partial t^2}u(x,y,z,t)=0\\ \Rightarrow\left[\frac{\partial^2}{\partial x^2}+\frac{\partial^2}{\partial y^2}+\frac{\partial^2}{\partial z^2}-\frac{1}{c^2}\frac{\partial^2}{\partial t^2}\right]u(x,y,z,t)\\ =\left[L_x^2+L_y^2+L_z^2-\frac{L_t^2}{c^2}\right]u=0\end{aligned} \tag{5.26}$$

and expanding the operators

$$Lu=\left[L_x^2+L_y^2+L_z^2-\frac{L_t^2}{c^2}\right]u=L^-L^+u=0 \tag{5.27}$$

where L^+ and L^- operators are

$$L^+=L_x+\frac{L_t}{c}\sqrt{1-\left(c\frac{L_y}{L_t}\right)^2-\left(c\frac{L_z}{L_t}\right)^2} \tag{5.28}$$

$$L^-=L_x-\frac{L_t}{c}\sqrt{1-\left(c\frac{L_y}{L_t}\right)^2-\left(c\frac{L_z}{L_t}\right)^2} \tag{5.29}$$

where the L^+ and L^- indicate the wave propagation on the right and left directions, respectively. No reflection is possible under below condition

$$L^+u|_{x=l_x}=0\,,\;\; L^-u|_{x=0}=0. \tag{5.30}$$

Because of the square root function, the L^+ and L^- operators are hard to solve exactly with the numerical methods [Enquist and Majda, 1977]. Therefore, instead of using

the square root function, its Taylor series expansion is used to obtain different ABCs [Mur, 1981].

5.6.2. First Order Mur ABC

Under $cL_y/L_t \ll 1$ and $cL_z/L_t \ll 1$ conditions the square root is approximately equal to 1 as

$$\sqrt{1-\left(c\frac{L_y}{L_t}\right)^2-\left(c\frac{L_z}{L_t}\right)^2} \cong 1 \tag{5.31}$$

where this situation shows that the derivatives on the directions y and z can be neglected. Accordingly, if the L^+ is rewritten at $x = 0$, L^+ becomes

$$L^+ = L_x + \frac{L_t}{c}\sqrt{1-\left(c\frac{L_y}{L_t}\right)^2-\left(c\frac{L_z}{L_t}\right)^2} \cong L_x - \frac{L_t}{c}. \tag{5.32}$$

Therefore, at $x = 0$ and $x = l_x$ boundaries, the first order Mur (FOMUR) ABC is obtained below

$$\begin{aligned} L^+u|_{x=l_x} = 0 \implies \frac{\partial}{\partial x}u|_{x=l_x} - \frac{1}{c}\frac{\partial}{\partial t}u|_{x=l_x} = 0 \\ L^-u|_{x=0} = 0 \implies \frac{\partial}{\partial x}u|_{x=0} - \frac{1}{c}\frac{\partial}{\partial t}u|_{x=0} = 0 \end{aligned} \tag{5.33}$$

If these equations are discretized, the FDTD update equations are

$$\begin{aligned} u|_{0,j,k}^{n+1} = u|_{1,j,k}^{n} + \frac{c\Delta t - \Delta x}{c\Delta t + \Delta x}\left(u|_{1,j,k}^{n+1} - u|_{0,j,k}^{n}\right) \\ u|_{N_x,j,k}^{n+1} = u|_{N_x-1,j,k}^{n} + \frac{c\Delta t - \Delta x}{c\Delta t + \Delta x}\left(u|_{N_x-1,j,k}^{n+1} - u|_{N_x,j,k}^{n}\right). \end{aligned} \tag{5.34}$$

For Maxwell's equations, these update equations are valid for the electric and magnetic fields. It is also sufficient to apply only the electric field components for termination [Mur, 1981].

5.6.3. Second Order Mur ABC

If the first two terms of the Taylor series expansion of the square root function in the OWWE are taken into account as

$$\sqrt{1-\left(c\frac{L_y}{L_t}\right)^2-\left(c\frac{L_z}{L_t}\right)^2}\cong 1-\frac{1}{2}\left[\left(c\frac{L_y}{L_t}\right)^2-\left(c\frac{L_z}{L_t}\right)^2\right] \tag{5.35}$$

where the second order accuracy is reached. Accordingly, if L^+ is rewritten at $x=l_x$, it becomes

$$\begin{aligned} L^+ &= L_x+\frac{L_t}{c}\sqrt{1-\left(c\frac{L_y}{L_t}\right)^2-\left(c\frac{L_z}{L_t}\right)^2} \\ &\cong L_x+\frac{L_t}{c}-\frac{c}{2L_t}\left(L_y^2+L_z^2\right). \end{aligned} \tag{5.36}$$

Therefore, at $x=0$ and $x=l_x$ boundaries, the second order accurate Mur (SOMUR) ABC is obtained like below

$$\begin{aligned} L^+u|_{x=l_x}=0 \;\Longrightarrow\; &\frac{\partial^2}{\partial x\partial t}u|_{x=l_x}+\frac{1}{c}\frac{\partial^2}{\partial t^2}u|_{x=l_x} \\ &-\frac{c}{2}\left(\frac{\partial^2}{\partial y^2}+\frac{\partial^2}{\partial z^2}\right)u|_{x=l_x}=0 \\ L^-u|_{x=0}=0 \;\Longrightarrow\; &\frac{\partial^2}{\partial x\partial t}u|_{x=0}-\frac{1}{c}\frac{\partial^2}{\partial t^2}u|_{x=0} \\ &+\frac{c}{2}\left(\frac{\partial^2}{\partial y^2}+\frac{\partial^2}{\partial z^2}\right)u|_{x=0}=0. \end{aligned} \tag{5.37}$$

If these equations are discretized, the FDTD update equations are

$$
\begin{aligned}
u|_{0,j,k}^{n+1} = -u|_{1,j,k}^{n} &+ \left(\frac{c\Delta t - \Delta x}{c\Delta t + \Delta x}\right)\left[u|_{1,j,k}^{n+1} + u|_{0,j,k}^{n}\right] \\
&+ \left(\frac{2\Delta x}{c\Delta t + \Delta x}\right)\left[u|_{1,j,k}^{n} + u|_{0,j,k}^{n}\right] \\
&+ \left(\frac{c^2\Delta t^2}{2\Delta x(c\Delta t + \Delta x)}\right)\left[u|_{1,j+1,k}^{n} - 4u|_{1,j,k}^{n}\right. \\
&+ u|_{1,j-1,k}^{n} + u|_{0,j+1,k}^{n} - 4u|_{0,j,k}^{n} \\
&+ u|_{0,j-1,k}^{n} + u|_{1,j,k+1}^{n} + u|_{1,j,k-1}^{n} \\
&\left.+ u|_{0,j,k+1}^{n} + u|_{0,j,k-1}^{n}\right]
\end{aligned}
\tag{5.38}
$$

and

$$
\begin{aligned}
u|_{N_x+1,j,k}^{n+1} = -u|_{N_x,j,k}^{n} &+ \left(\frac{c\Delta t - \Delta x}{c\Delta t + \Delta x}\right)\left[u|_{N_x,j,k}^{n+1} + u|_{N_x+1,j,k}^{n}\right] \\
&+ \left(\frac{2\Delta x}{c\Delta t + \Delta x}\right)\left[u|_{N_x,j,k}^{n} + u|_{N_x+1,j,k}^{n}\right] \\
&+ \left(\frac{c^2\Delta t^2}{2\Delta x(c\Delta t + \Delta x)}\right)\left[u|_{N_x,j+1,k}^{n}\right. \\
&- 4u|_{N_x,j,k}^{n} + u|_{N_x,j-1,k}^{n} + u|_{N_x+1,j+1,k}^{n} \\
&- 4u|_{N_x+1,j,k}^{n} + u|_{N_x+1,j-1,k}^{n} + u|_{N_x,j,k+1}^{n} \\
&+ u|_{N_x,j,k-1}^{n} + u|_{N_x+1,j,k+1}^{n} \\
&\left.+ u|_{N_x+1,j,k-1}^{n}\right].
\end{aligned}
\tag{5.39}
$$

For the solution of the two and three dimensional problems, the second order accurate Mur ABC does not work at the corners [Yang and Liou, 1998]. Therefore, the first order Mur ABC must be used at the corners.

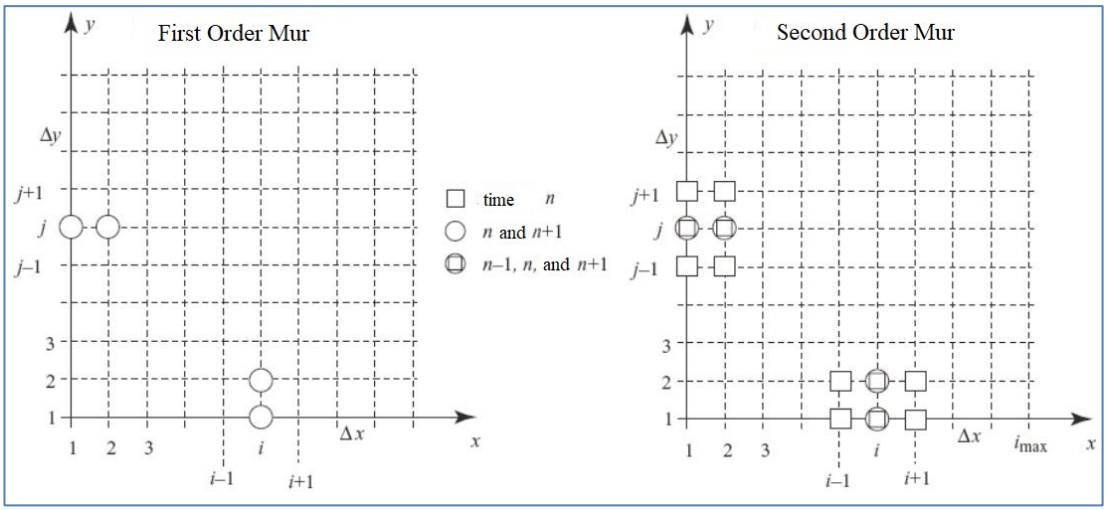

Figure 5.3: Mesh diagrams for the first and second order Mur ABCs.

5.6.4. Modified Mur ABC

The modified Mur ABC is an alternate form of the classical second order Mur ABC [Arabi and Mittra, 1995].

Manipulating the approximation of the OWWE, we can rewrite it as

$$\left(\frac{\partial u}{\partial x}-\frac{1}{c}\frac{\partial u}{\partial t}\right)\left(\frac{\partial u}{\partial x}-\frac{1}{c}\frac{\partial u}{\partial t}\right)=0 \tag{5.40}$$

where note that this equation involves only the normal derivatives. If this equation is discretized, the FDTD update equation at $x=0$ is

$$\begin{aligned} u|_{0,j,k}^{n+1} = {} & 2u|_{1,j,k}^{n}-u|_{2,j,k}^{n-1} \\ & -2K_x\left[u|_{0,j,k}^{n}-u|_{1,j,k}^{n+1}-u|_{1,j,k}^{n-1}+u|_{2,j,k}^{n}\right] \\ & -K_x^2\left[u|_{0,j,k}^{n-1}+u|_{2,j,k}^{n+1}-2u|_{1,j,k}^{n}\right] \end{aligned} \tag{5.41}$$

where $K_x=(c\Delta t-\Delta x)/(c\Delta t+\Delta x)$. This form of the modified Mur ABC has some advantages:

- It is computationally simpler than the conventional SOMUR ABC,
- It has no tangential derivatives, therefore it works at the corners,

- It has higher accuracy than the conventional SOMUR ABC.

There is also another study to overcome long time instability problem of the second order Mur ABC. For this aim, *upwind* finite differences are used instead of the central differences approximation [Yusheng and Wenbing, 1996].

5.6.5. Performance of the Mur ABCs

The reflection errors of the first, second, modified and upwind finite difference of Mur ABC are shown in Figure 5.4. A wideband pulse is used for the excitation of a magnetic dipole source located at the center of the FDTD mesh in the lossy medium. The results show that the modified Mur ABC has the lowest reflection error.

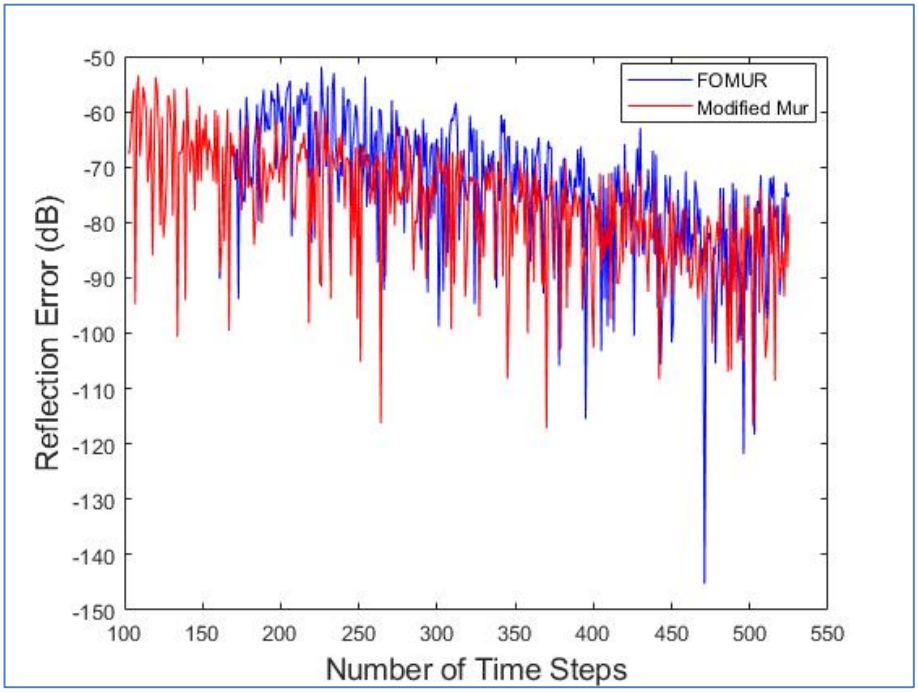

a)

Figure 5.4: The reflection error comparisons of the modified Mur with a) the FOMUR, b) the conventional SOMUR and c) the upwind SOMUR.

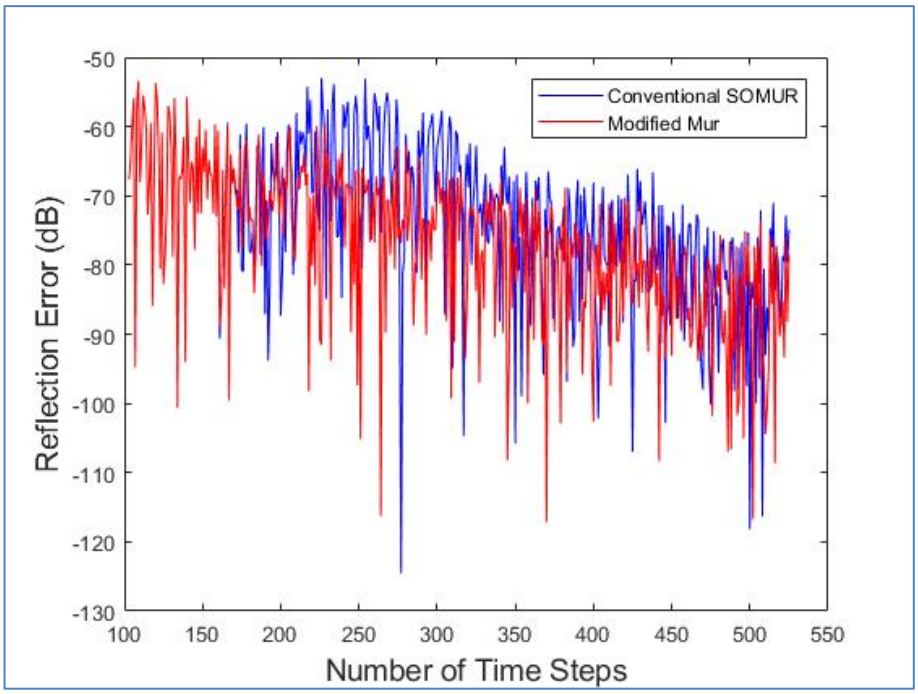

b)

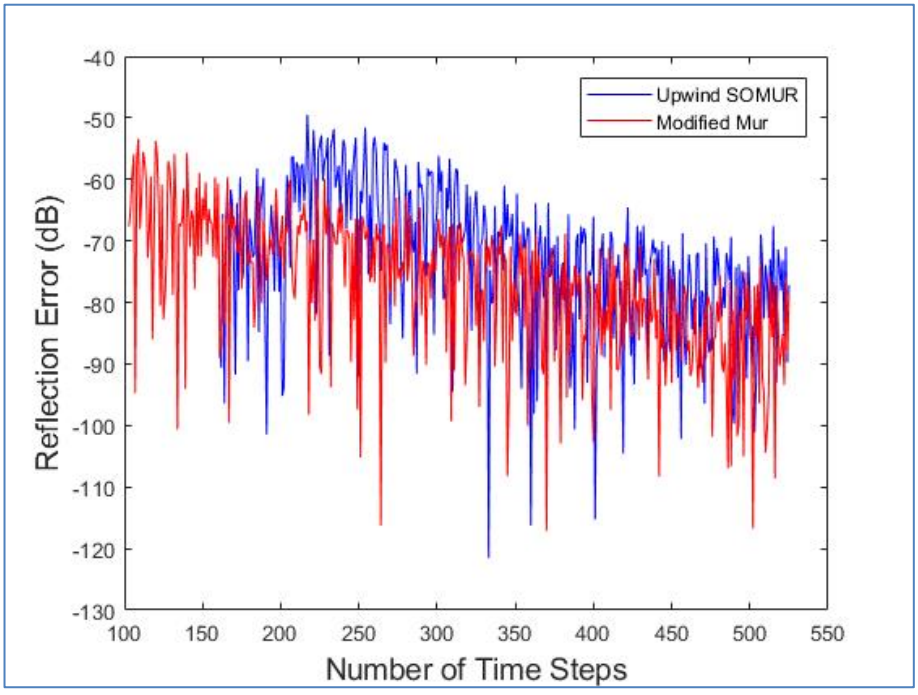

c)

Figure 5.4: Continuation.

It is also observed in Table 5.1, the modified Mur ABC requires less computational time than the other second order Mur ABCs. Therefore, the modified Mur ABC is preferred in this study.

Table 5.1: The computational times for the four different Mur ABC types.

	FOMUR	Conventional SOMUR	Upwind SOMUR	Modified Mur
Computational Time (s)	108.507	112.431	111.446	110.435

5.7. Quasi-Static FDTD Method

In the low frequency metal detector problem, the wavelength is far bigger than the buried object dimensions. This gives rise to a limitation that the classical FDTD unit cell size must be too smaller than the wavelength. This leads to the extremely small FDTD time step because of the CFL stability criterion. Therefore, to run the classical FDTD method for a full period of time, it is required unsuitable computational times such as years with todays' computer technology. To overcome this limitation, a Quasi-Static FDTD (QS-FDTD) method is proposed and valid for quasi-static approximation.

There are two types of the quasi-static approximations based on neglecting displacement currents and magnetic induction currents which are known as Magneto-Quasi-Static (MQS) and Electro-Quasi-Static (EQS), respectively.

In the metal detectors, the displacement currents on the metal object are smaller than the conduction currents. Therefore, the MQS condition is valid. In the time domain, this condition is shown as below

$$\frac{\partial}{\partial t}\vec{D}(\vec{r},t) \ll \sigma\vec{E}(\vec{r},t). \tag{5.42}$$

In the simple lossy medium, this condition becomes in the frequency domain for the monochromatic wave

$$j\omega\varepsilon\vec{E}(\vec{r}) \ll \sigma\vec{E}(\vec{r}) \quad \Longrightarrow \quad |j\omega\varepsilon \ll \sigma| \quad \Longrightarrow \quad 2\pi f\varepsilon \ll \sigma. \tag{5.43}$$

Under this condition, if the displacement currents are completely neglected, the wave equation turns into the diffusion equation. However, in the QS-FDTD method, the displacement currents are kept under the MQS condition and the propagation velocity is slowed down by scaling up the dielectric permittivity. Therefore, the FDTD unit time step becomes bigger and it makes the problem solvable in reasonable computational times [Özakın and Aksoy, 2016].

Effects of the MQS approximation on the fundamental parameters are analyzed below.

1) Propagation Constant: The propagation constant in the lossy medium is

$$k = k_{real} + jk_{imag} = \sqrt{\omega^2 \varepsilon \mu + j\omega\sigma\mu} \tag{5.44}$$

where the real part (k_{real}) and imaginary part (k_{imag}) can be expressed as

$$k_{real} = \underbrace{\sqrt{\varepsilon_0\mu_0}}_{k_0} \underbrace{\sqrt{\varepsilon_r\mu_r}\left(\frac{1}{2}\left[\sqrt{1+\left(\frac{\sigma}{\omega\varepsilon_0\varepsilon_r}\right)^2}+1\right]\right)^{1/2}}_{\sqrt{\alpha_k}} \tag{5.45}$$

$$k_{imag} = \underbrace{\sqrt{\varepsilon_0\mu_0}}_{k_0} \sqrt{\varepsilon_r\mu_r}\left(\frac{1}{2}\left[\sqrt{1+\left(\frac{\sigma}{\omega\varepsilon_0\varepsilon_r}\right)^2}-1\right]\right)^{1/2} \tag{5.46}$$

where k_{real} models the wave propagation phenomenon and it is $\sqrt{\alpha_k}$ times bigger than the propagation constant (k_0) in the free space. Therefore, the propagation velocity c in the lossy medium reduces as

$$c = \frac{\omega}{k_{real}} = \frac{\omega}{\sqrt{\alpha_k}k_0} = \frac{1}{\sqrt{\alpha_k}}c_0 \tag{5.47}$$

where $c \ll c_0$. This fact shows that the velocity of propagation in the lossy medium slows down.

If k_{real} and k_{imag} are equal, the displacement currents are completely neglected. Then

$$k \cong \sqrt{j\omega\mu\sigma} \implies k_{real} = k_{imag} \cong \sqrt{\frac{\omega\mu\sigma}{2}} \tag{5.48}$$

where this condition leads to the diffusion equation.

2) Skin Depth: The skin depth δ is

$$\delta = \frac{1}{k_{real}} = \frac{1}{\sqrt{\varepsilon_0\mu_0}\sqrt{\varepsilon_r\mu_r}\left(\frac{1}{2}\left[\sqrt{1+\left(\frac{\sigma}{\omega\varepsilon_0\varepsilon_r}\right)^2}+1\right]\right)^{1/2}}. \tag{5.49}$$

Under the MQS condition it becomes

$$k_{real} \cong \sqrt{\frac{\omega\mu\sigma}{2}} \implies \delta = \frac{1}{k_{real}} \cong \sqrt{\frac{2}{\omega\mu\sigma}}. \tag{5.50}$$

3) Impedance: The wave impedance in the lossy medium is

$$Z = \frac{|\vec{E}|}{|\vec{H}|} = \sqrt{\frac{\mu}{\varepsilon + j\frac{\sigma}{\omega}}} \tag{5.51}$$

and Z can also be approximated with neglecting the displacement currents as

$$Z = \frac{|\vec{E}|}{|\vec{H}|} = \sqrt{\frac{\mu\omega}{j\sigma}}. \tag{5.52}$$

4) Critical Model Time Parameters and Continuity Equation: Three time constants must be considered in the MQS problems: The relaxation time ($\tau_e = \varepsilon/\sigma$), the transmit time ($\tau_t = L\sqrt{\varepsilon\mu}$), and the magnetic diffusion time ($\tau_m = \sigma\mu L^2$) where L is

the characteristic dimension of the object. In the MQS approximation, the following condition must be satisfied in the lossy media

$$\tau_e < \tau_t < \tau_m. \tag{5.53}$$

To analyze the numerical behavior of the FDTD method in the lossy medium, it is necessary to extract the numerical wave number (k^N)

$$k^N = \omega\sqrt{\varepsilon_N \mu} = \omega\sqrt{\left(\varepsilon + j\frac{\sigma\Delta t}{2\tan(\omega\,\Delta t/2)}\right)\mu} \tag{5.54}$$

where ε_N is the numerical dielectric permittivity. The real and imaginary parts of k^N are

$$k^N_{real} = k_0\sqrt{\varepsilon_r\mu_r}\left(\frac{1}{2}\sqrt{1+\left(\frac{\sigma}{\omega\varepsilon_0\varepsilon_r}\right)^2\left(\frac{\omega\,\Delta t/2}{\tan(\omega\,\Delta t/2)}\right)^2}+1\right)^{1/2} \tag{5.55}$$

$$k^N_{imag} = k_0\sqrt{\varepsilon_r\mu_r}\left(\frac{1}{2}\sqrt{1+\left(\frac{\sigma}{\omega\varepsilon_0\varepsilon_r}\right)^2\left(\frac{\omega\,\Delta t/2}{\tan(\omega\,\Delta t/2)}\right)^2}-1\right)^{1/2} \tag{5.56}$$

where $\tan(\omega\,\Delta t/2) \cong \omega\,\Delta t/2$ for small argument approximation. Thus, k^N_{real} and k^N_{imag} are

$$k^N_{real} \cong k_0\sqrt{\varepsilon_r\mu_r}\left(\frac{1}{2}\sqrt{1+\left(\frac{\sigma}{\omega\varepsilon_0\varepsilon_r}\right)^2}+1\right)^{1/2} \implies k^N_{real} = k_{real} \tag{5.57}$$

$$k^N_{imag} \cong k_0\sqrt{\varepsilon_r\mu_r}\left(\frac{1}{2}\sqrt{1+\left(\frac{\sigma}{\omega\varepsilon_0\varepsilon_r}\right)^2}-1\right)^{1/2} \implies k^N_{imag} = k_{imag} \tag{5.58}$$

where it is clear that the numerical wave number is equal to the analytical wave number.

In the FDTD numerical solution, the propagation velocity slows down because $k^N > k_0$. However, the slowed propagation velocity does not affect Δt in the classical FDTD method because the stability condition depends on c_0, not the slowed c. Therefore, it is necessary to use a material scaling technique. The material scaling technique can be applied by scaling the parameters ε, μ, σ and ω. However, only the ε-scaling is feasible for the FDTD solution.

To find a proper value for the scaling factor, its effects on the following critical parameters and conditions must be analyzed:

i) The QS and MQS conditions,
ii) Parameters of τ_e, τ_t and τ_m,
iii)Parameters of δ, Z and rescaling,
iv)Numerical dispersion and stability.

i) QS Condition and k: The scaling does not strongly affect the QS condition and k because k_{real} is not strongly depend on ε.
ii) MQS Condition: The MQS condition is directly affected by the scaling. Therefore, the scaling factor must obey the following criterion

$$2\pi f \alpha_{MQS} \varepsilon \ll \sigma \quad \Longrightarrow \quad \alpha_{MQS} \ll \frac{\sigma}{2\pi f \varepsilon}. \tag{5.59}$$

iii) τ_e, τ_t *and* τ_m*:* To model the MQS condition properly in the QS-FDTD method, the modified unit time step Δt^{QS} must satisfy the following condition

$$\Delta t^{QS} < \tau_e^{QS} < \tau_t^{QS} < \tau_m \tag{5.60}$$

where τ_e^{QS} and τ_t^{QS} are the changed forms of τ_e and τ_t after the ε-scaling. Furthermore, τ_m is not affected by the scaling. These limitations can be analyzed one by one as follows.

The first case:

$$\Delta t^{QS} = \sqrt{\alpha}\Delta t < \tau_e^{QS} = \alpha\tau_e \implies \alpha_{\Delta t} > \left(\frac{\Delta t}{\tau_e}\right)^2 \tag{5.61}$$

where, τ_e^{QS} reduces for the very high conductive objects. This strongly limits the QS-FDTD unit time step. Therefore, the transient charge calculation using the QS-FDTD method for the high conductive objects is not feasible.

The second and third cases have same limitation:

$$\tau_e^{QS} < \tau_t^{QS} \implies \alpha\tau_e < \sqrt{\alpha\tau_e\tau_m} \implies \alpha = \alpha_\tau < \frac{\tau_m}{\tau_e} \tag{5.62}$$

$$\tau_t^{QS} < \tau_m \implies \sqrt{\alpha\tau_e\tau_m} < \tau_m \implies \alpha = \alpha_\tau < \frac{\tau_m}{\tau_e} \tag{5.63}$$

iv) δ , Z and Rescaling: The skin depth can be approximated as $\delta = 1/k_{real} \cong (2/\omega\sigma\mu)^{1/2}$. Therefore, δ is weakly affected by the ε-scaling. The wave impedance is affected by the ε-scaling

$$Z^{QS} = \frac{|E|^{QS}}{|H|^{QS}} = \sqrt{\frac{\mu}{\alpha\varepsilon + j\frac{\sigma}{\omega}}}; \quad Z = \sqrt{\frac{\mu}{\varepsilon + j\frac{\sigma}{\omega}}} \tag{5.64}$$

where Z^{QS} is the scaled and Z is the unscaled wave impedance. Under the MQS condition, they can be approximated as

$$Z = \sqrt{\frac{\mu}{\varepsilon}}\sqrt{\frac{1}{1 + j\frac{\sigma}{\omega\varepsilon}}} \cong Z_0\sqrt{\frac{1}{j\frac{\sigma}{\omega\varepsilon}}} \tag{5.65}$$

and

$$Z^{QS} = Z_0\sqrt{\frac{1}{\alpha + j\frac{\sigma}{\omega\varepsilon}}} = Z_0\sqrt{\frac{1}{j\frac{\sigma}{\omega\varepsilon}}}\sqrt{\frac{1}{1 + \alpha\frac{\omega\varepsilon}{j\sigma}}} \tag{5.66}$$

where Z_0 is the wave impedance in the free space. Under the MQS condition, $|\alpha\omega\varepsilon/j\sigma| \ll 1$ is true. Using the generalized binomial expansion, Z^{QS} can be approximated as

$$Z^{QS} = Z\sqrt{\frac{1}{1+\alpha\frac{\omega\varepsilon}{j\sigma}}} \cong Z\frac{1}{1+\frac{1}{2}\alpha\frac{\omega\varepsilon}{j\sigma}} = \frac{Z}{\alpha'} \tag{5.67}$$

where α' is the rescaling factor between Z^{QS} and Z. The rescaling factor depends on the problem type. If the source is an electric field type, the magnetic field must be scaled up by $|\alpha'|$. Therefore, the magnetic field must be rescaled by $|\alpha'|$. If the source is the magnetic field type, the electric field must be scaled up by $|\alpha'|$. Therefore, the electric field must be rescaled by $|\alpha'|$.

v) Numerical Stability and Dispersion: The QS-FDTD stability criterion is the same as the classical FDTD method below

$$\frac{c^{QS}\Delta t^{QS}}{\Delta x^{QS}} \leq 1 \implies \Delta t^{QS} \leq \frac{\Delta x^{QS}}{c^{QS}} = \sqrt{\alpha}\frac{\Delta x}{c_0} \leq \sqrt{\alpha}\Delta t. \tag{5.68}$$

Nyquist sampling limitation is also important factor in the QS-FDTD method. Δt must be smaller than the Nyquist unit time step Δt_N

$$\Delta t \leq \Delta t_N = \frac{1}{2f_{max}} \tag{5.69}$$

where f_{max} is the maximum frequency value. After the scaling, Δt becomes $\Delta t^{QS} = \sqrt{\alpha}\Delta t$, and the Nyquist criterion must be again satisfied as

$$\Delta t^{QS} = \sqrt{\alpha}\Delta t \leq \Delta t_N = \frac{1}{2f_{max}} \implies \alpha_N \leq \left(\frac{1}{2f_{max}\Delta t}\right)^2. \tag{5.70}$$

To choose the proper value of α under all these considerations, a flowchart is developed in Figure 5.5.

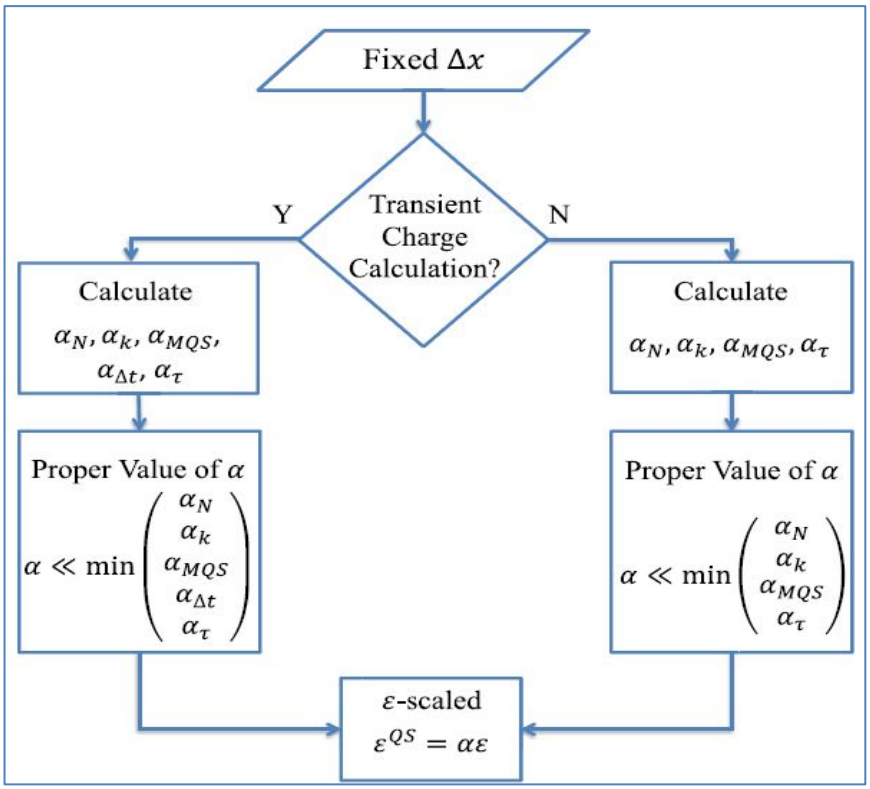

Figure 5.5: The flowchart for the selection of the scaling factor.

In Table 5.2, it is also shown how the scaling affects these parameters.

Table 5.2: Effect of the scaling factor on the critical parameters.

Parameters	**Effect of the ε-scaling**
$k = \sqrt{\omega^2\varepsilon\mu + j\omega\mu\sigma}$	Weakly affected
$Z = \sqrt{\mu/(\varepsilon + j(\sigma/\omega))}$	Weakly affected
$c = 1/\sqrt{\varepsilon\mu}$	Reduced
$\delta = 1/k_{real}$	Weakly affected
$\tau_e = \varepsilon/\sigma$	Increased
$\tau_t = L\sqrt{\varepsilon\mu}$	Increased
$\tau_m = \mu\sigma L^2$	Not affected
$\nabla \cdot E(r,t) = \rho/\varepsilon$	Affected

5.8. Validation of the QS-FDTD Method

5.8.1. Pattern Calculation of a Magnetic Dipole

In the electromagnetic induction problems, the loop antennas are generally used as a sensor. In this study, instead of the loop antenna, its equivalent magnetic dipole model is used for simplicity. This equivalence for an infinitesimal magnetic dipole of length l and spatial magnetic current I_m can be shown as

$$I_m l = jS\omega\mu I_0 \tag{5.71}$$

where S and I_0 are the area and current of the loop, respectively [Balanis, 2005].

Analytical solution of an infinitesimal magnetic dipole is given in the near field region ($kr \ll 1$) as

$$\begin{aligned}
H_r &\cong \frac{I_m l \cos\theta}{2\pi\eta r^2}\left(1+\frac{1}{jkr}\right)e^{-jkr} \\
H_\theta &\cong j\frac{kI_m l \sin\theta\, e^{-jkr}}{4\pi\eta r}\left(1+\frac{1}{jkr}-\frac{1}{(kr)^2}\right)e^{-jkr} \\
H_\phi &= 0 \\
E_r &= 0 \\
E_\theta &= 0 \\
E_\phi &\cong -j\frac{kI_m l \sin\theta}{4\pi r}\left(1+\frac{1}{jkr}\right)e^{-jkr}
\end{aligned} \tag{5.72}$$

The near field patterns of the magnetic and electric field components are calculated in the Cartesian coordinates using the QS-FDTD method and validated with the analytical solution [Özakın and Aksoy, 2017]. In Figure 5.6 and Figure 5.7 the three dimensional patterns of each field components are shown for the analytical solution and QS-FDTD solution, respectively. A good agreement is observed between the QS-FDTD and analytical solutions.

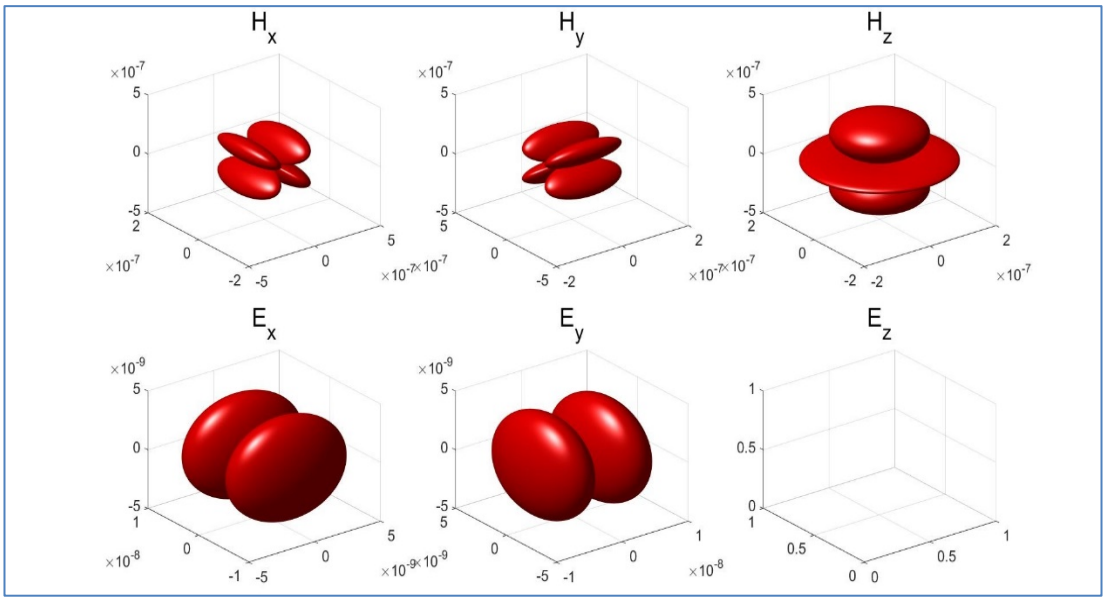

Figure 5.6: The analytical near field pattern of the magnetic dipole.

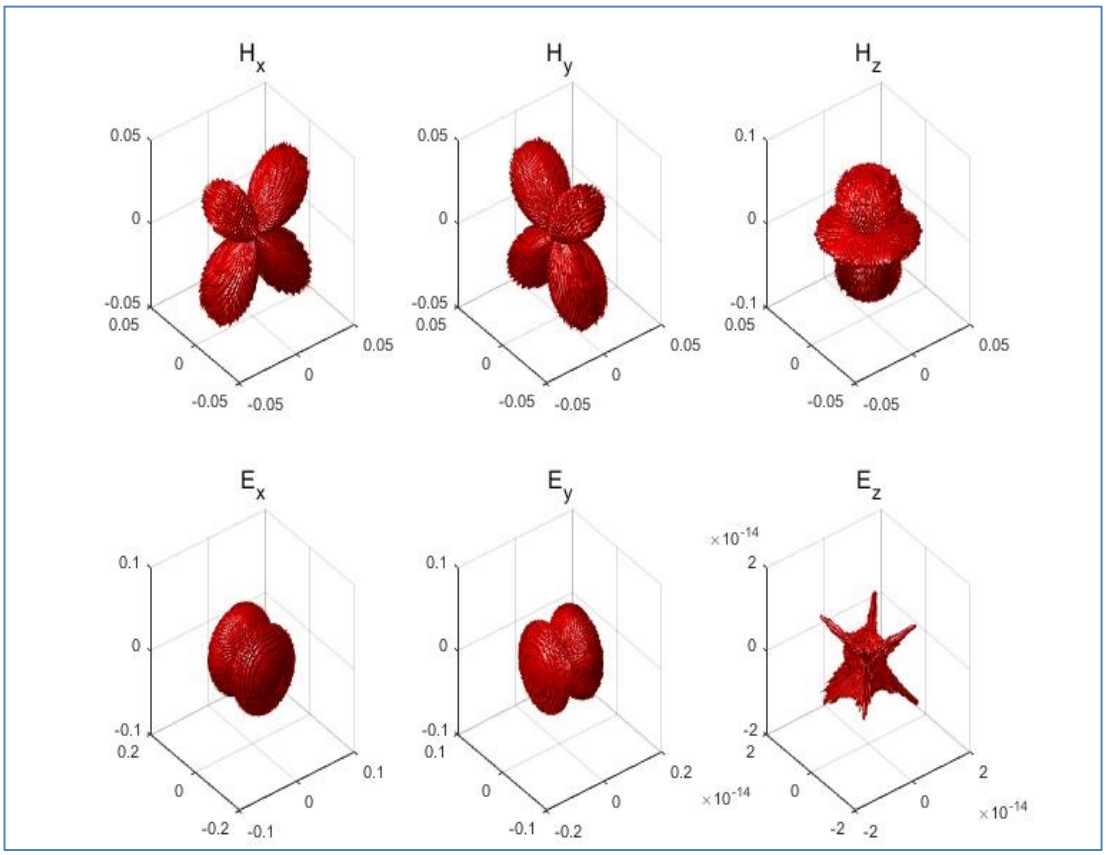

Figure 5.7: The numerical near field pattern of the magnetic dipole.

5.8.2. I/Q Signature Calculation

To validate the QS-FDTD method, Wait's analytical solution of scattered fields from a high conducting sphere located in a poorly conducting medium is used with a homogeneous magnetic field excitation [Wait, 1951]. The Phase (I) and Quadrature (Q) component of the scattered field are calculated in the frequency domain. In the Wait's solution the displacement currents are neglected in the sphere region but they are kept in the QS-FDTD solution. The analytical I and Q values are given as

$$I + jQ = \frac{1}{\beta^2} + \frac{1}{3} - \frac{\cosh\beta}{\beta \sinh\beta} \tag{5.73}$$

and

$$\beta = \sqrt{j\sigma_1\mu_1\omega - \varepsilon_1\mu_1\omega^2} \tag{5.74}$$

where $\varepsilon_1 = \varepsilon_0$, $\mu_1 = \mu_0$ and $\sigma_1 = 10^6$ S/m are the dielectric permittivity, magnetic permeability and conductivity of the sphere, respectively. The radius of the sphere is taken as 1 m.

In Figure 5.8, it is clearly seen that there is a good agreement between the Wait's analytical solution and the QS-FDTD solution at the low and medium frequencies. There is a small deflection for I component at the higher frequencies. It is thought that there can be many reasons of this deflection; negligence of the displacement currents in the sphere region or exact homogeneous wave excitation in analytical solution.

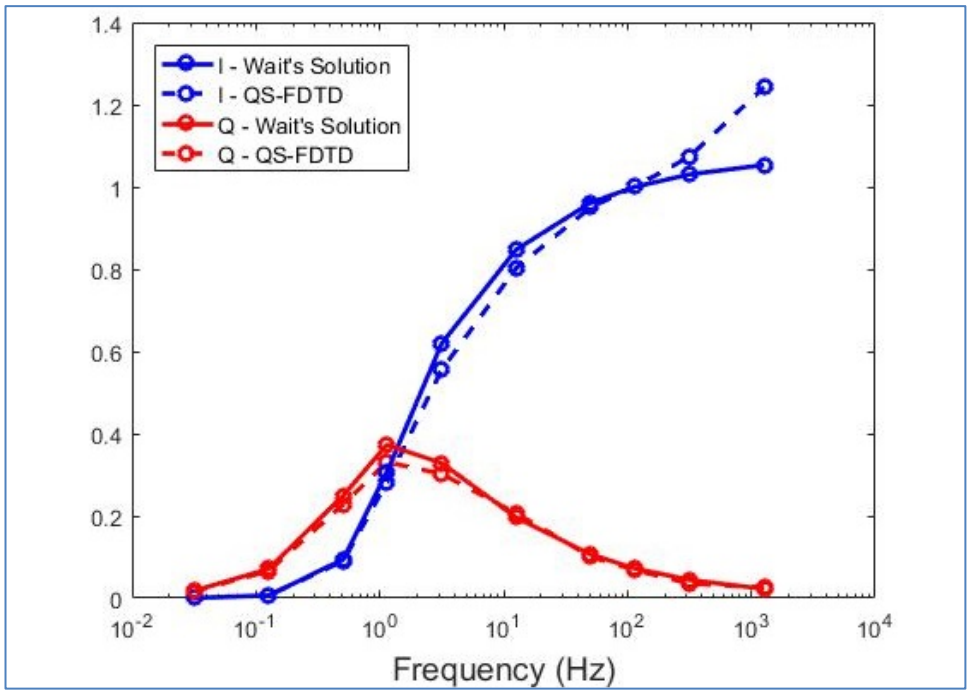

Figure 5.8: The I/Q signature of the conducting sphere.

6. NUMERICAL EXAMPLE

Time signatures of a buried cubic metallic object and a buried cubic air gap are investigated for different positions of the antenna and object. The scattered fields are calculated by subtraction of the incident fields from the total fields. The magnetic dipole model is used for excitation.

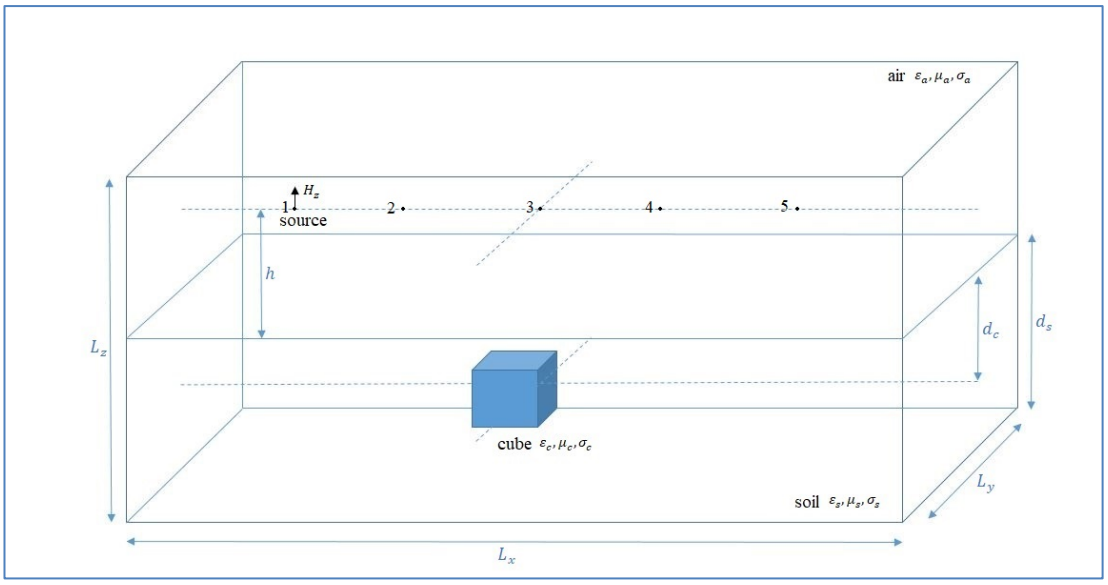

Figure 6.1: The 3D problem space.

The geometry of the problem is shown in Figure 6.1. Here, L_x, L_y and L_z are the dimensions of the problem space on the directions of x, y and z, respectively. h shows the height of the source, d_p is the depth of the soil and d_c is the depth of the cube. The magnetic dipole on the z direction is used as the excitation source. All the geometrical and physical parameters of this problem are listed in Table 6.1. The applied current pulse waveform and its frequency spectrum are shown in Figure 6.2. The bandwidth of the pulse signal is about 10 kHz. In the FDTD solution, to a strong numerical dispersion is observed in the transient part of the wideband response of the source signal. To solve this problem, an advanced adaptive filter of Butterworth type is used.

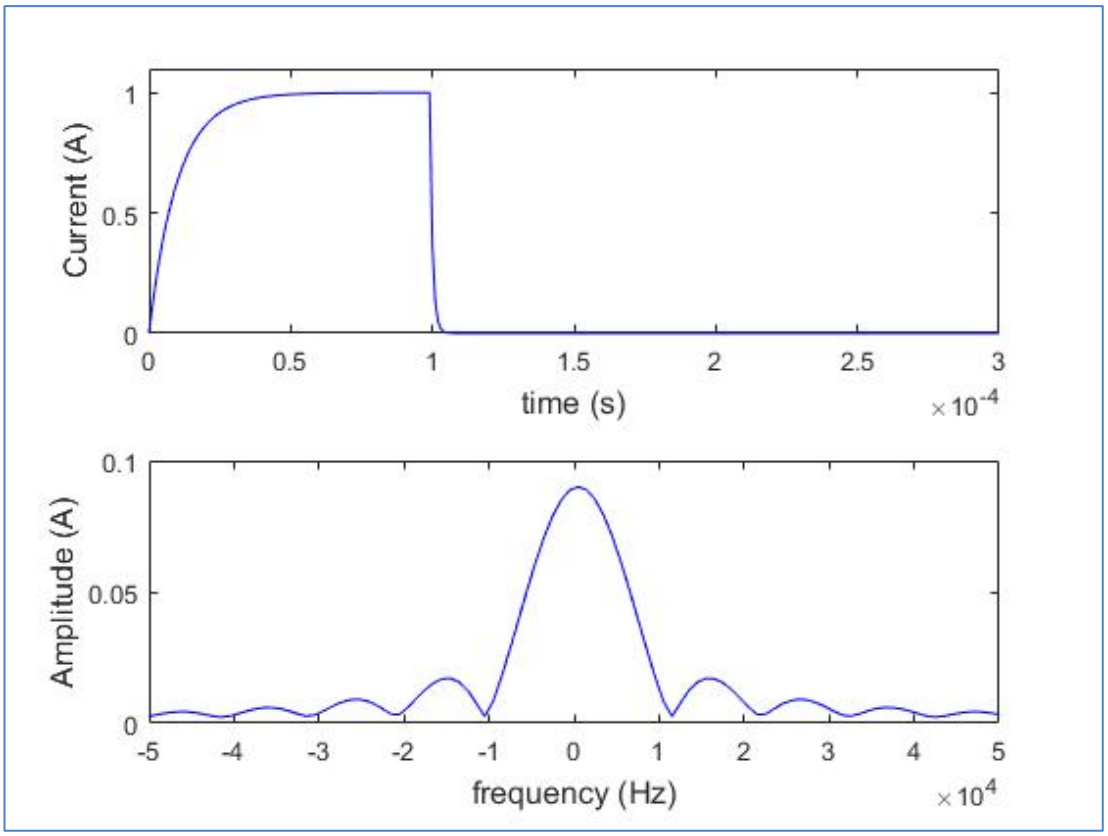

Figure 6.2: The applied current pulse waveform and its frequency spectrum.

Table 6.1: The geometrical and physical parameters used in the QS-FDTD solution.

Parameter	Value	Unit	Definition
L_x	1.40	m	Length on the direction of x
L_y	0.30	m	Length on the direction of y
L_z	0.75	m	Length on the direction of z
d_s	0.50	m	Depth of the soil
Δx	0.01	m	Unit cell size on the direction of x
Δy	0.01	m	Unit cell size on the direction of y
Δz	0.01	m	Unit cell size on the direction of z
N_x	140	-	Number of cells on the direction of x
N_y	30	-	Number of cells on the direction of y
N_z	75	-	Number of cells on the direction of z
α	5×10^8	-	QS-FDTD scaling factor
ε_0	$10^{-9}/(36\pi)$	F/m	Dielectric permittivity in the free space
μ_0	$4\pi \times 10^{-7}$	H/m	Magnetic permeability in the free space

Table 6.1: Continuation.

ε_{air}^{QS}	$\alpha \times \varepsilon_0$	F/m	Scaled dielectric permittivity of the air
μ_{air}	μ_0	H/m	Magnetic permeability of the air
σ_{air}	5.56×10^{-3}	S/m	Conductivity of the air
ε_{soil}^{QS}	$\alpha \times 1.5 \times \varepsilon_0$	F/m	Scaled dielectric permittivity of the soil
μ_{soil}	μ_0	H/m	Magnetic permeability of the soil
σ_{soil}	8.33×10^{-3}	S/m	Conductivity of the soil
ε_{cube}^{QS}	$\alpha \times 2.5 \times \varepsilon_0$	F/m	Scaled dielectric permittivity of the cube
μ_{cube}	μ_0	H/m	Magnetic permeability of the cube
σ_{cube}	1×10^6	S/m	Conductivity of the cube
Δt^{QS}	4.3053×10^{-10}	sn	QS-FDTD unit time step
T	696824	-	Total number of iteration

6.1. Buried Metal Cube

The effects of the height of the source h and depth of the cube d_c are investigated for the buried metal cube. The side length of the cube is set to 0.1 m and located at the middle of the x axis. The calculations are made for five times with five different locations of the source on the x axis (1, 2, 3, 4 and 5 locations in Figure 6.1). The time domain data is collected at the source location.

The effects of the antenna height and location; the object depth, size, orientation, shape and material type can be analyzed by decay curve and amplitude of the voltage response. In this work, the voltage responses are extracted at the different antenna heights and horizontal locations and different object depths for air filled and aluminum cubic objects.

6.1.1. Effect of the Source Height

In Figure 6.3, the magnetic field strength and induced voltage in the time domain are shown at $h = 10$ cm and $d_c = 20$ cm for location 3. The voltage value is

obtained by differentiating the magnetic field strength. The voltage response is used for the analysis.

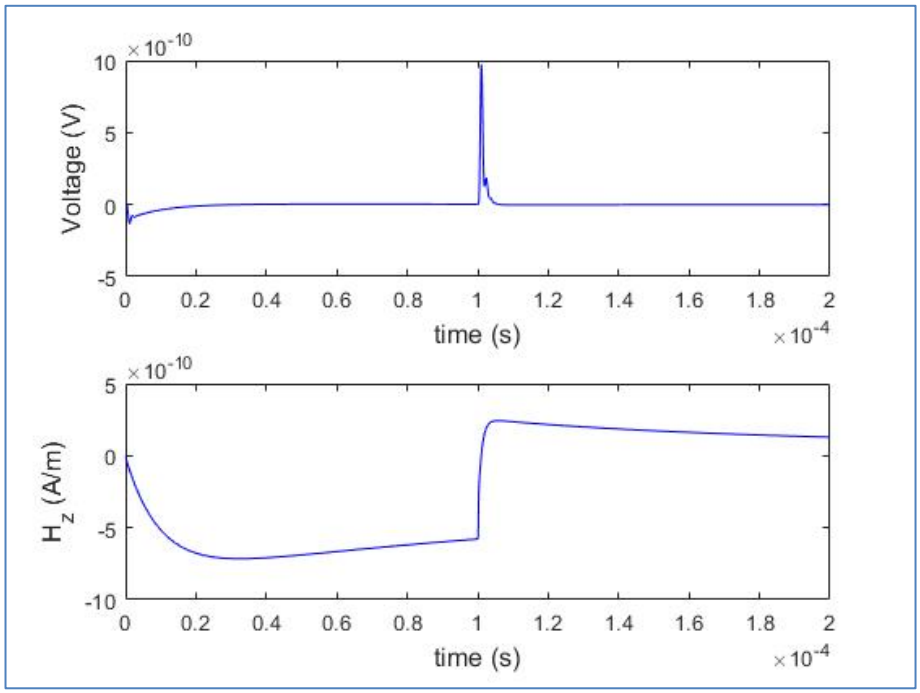

Figure 6.3: The time domain scattered magnetic field (H_z) and voltage response.

Two calculations are made at the two heights of the source $h = 10$ cm and 20 cm for the fixed object depth $d_c = 20$ cm. The source located at location 3 on the x axis. Figure 6.4 shows that the source height affects only the amplitude of the voltage response, not the decay time. The dispersion caused by the pulse type signal is stronger for sources located at the higher height. Therefore, it is difficult to filter raw data for obtaining the clear response.

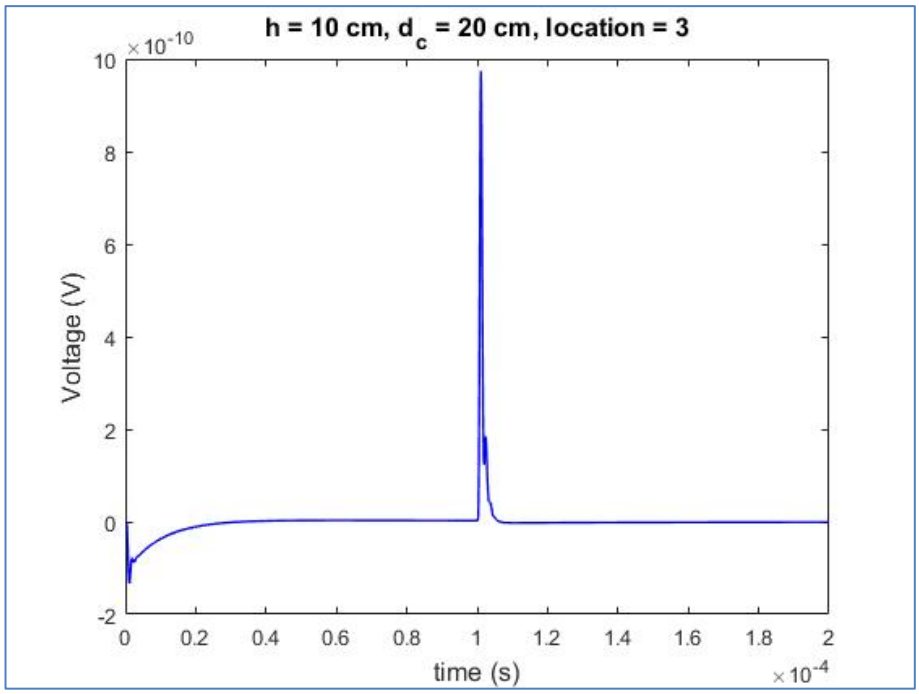

a)

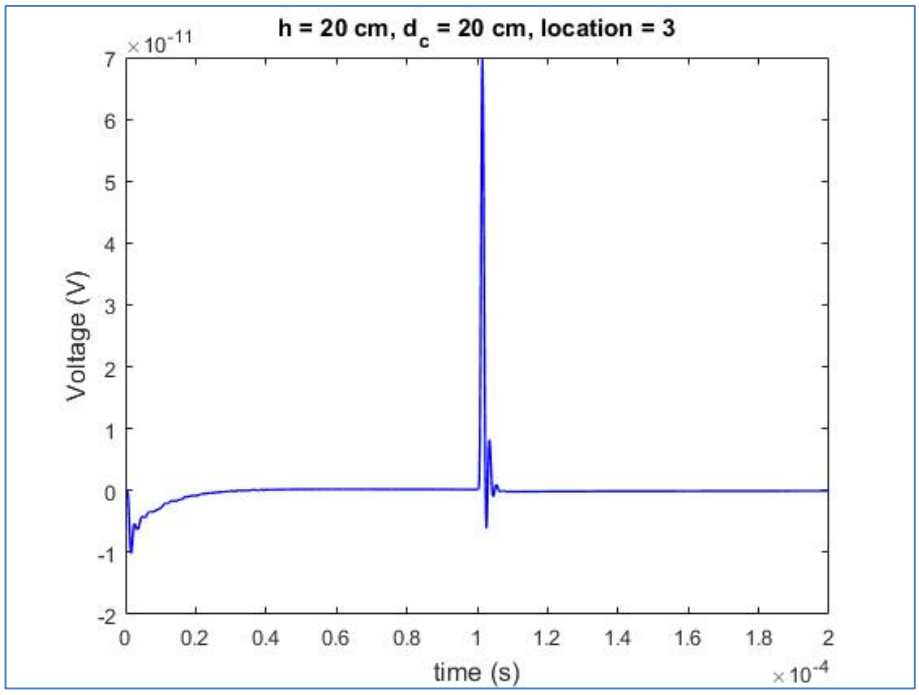

b)

Figure 6.4: The time domain voltage responses for the metal cube at a) $h = 10$ cm and b) $h = 20$ cm.

6.1.2. Effect of the Object Depth

Three calculations are performed at the three depths of the object $d_c = 10$ cm, 20 cm and 30 cm for the fixed source height $h = 10$ cm. The source located at location 3 on the x axis. Figure 6.5 shows that the object depth affects only the amplitude of the voltage response, not the decay time. The numerical dispersion caused by the pulse type signal is stronger for the objects buried deeper. Therefore, it is difficult to filter for obtaining the clear response.

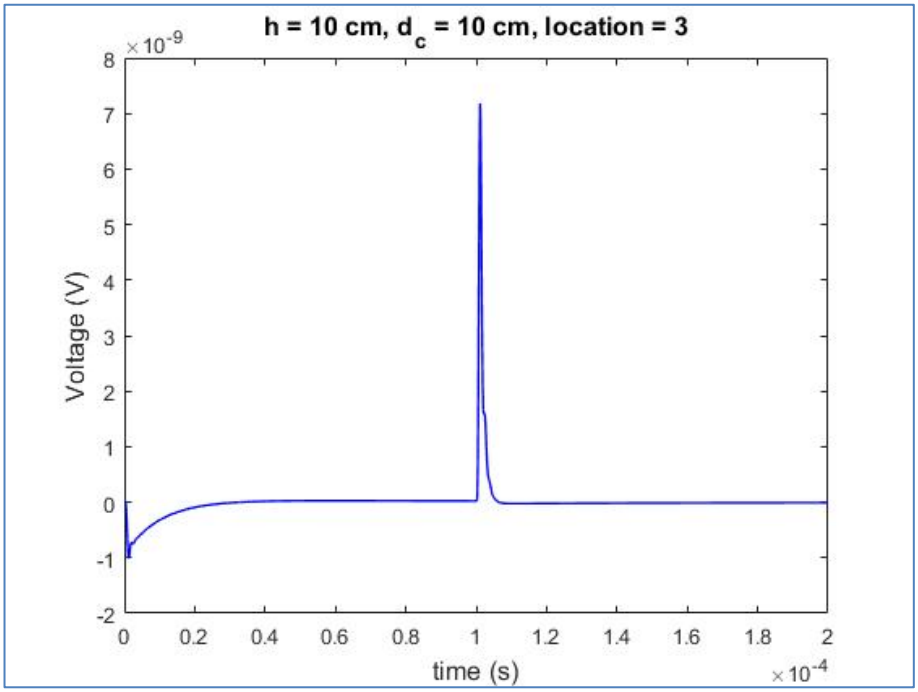

a)

Figure 6.5: The time domain voltage responses for the buried metal cube at a) $d_c = 10$ cm, b) $d_c = 20$ cm and c) $d_c = 30$ cm.

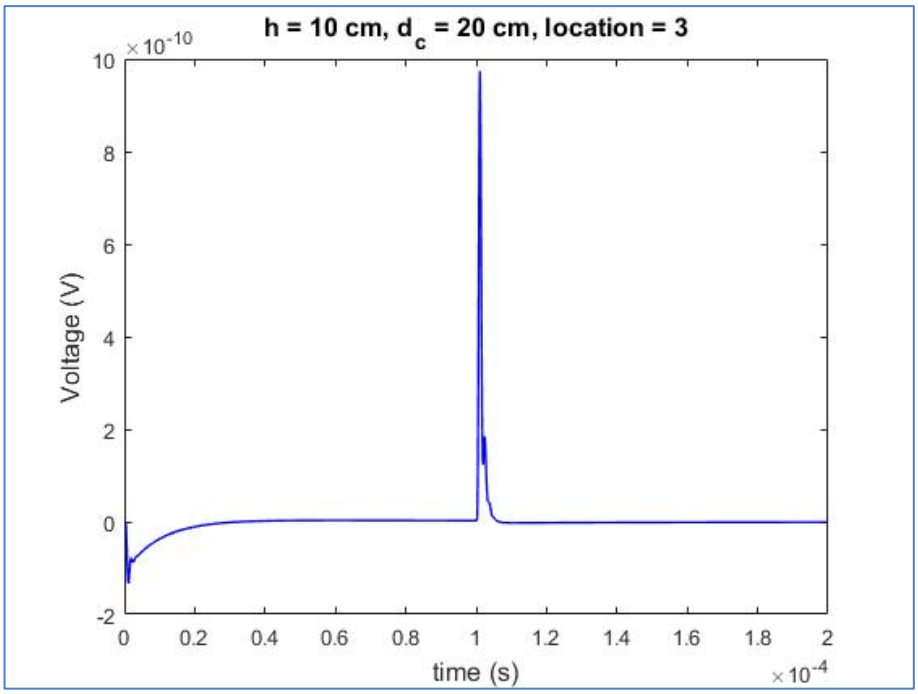

b)

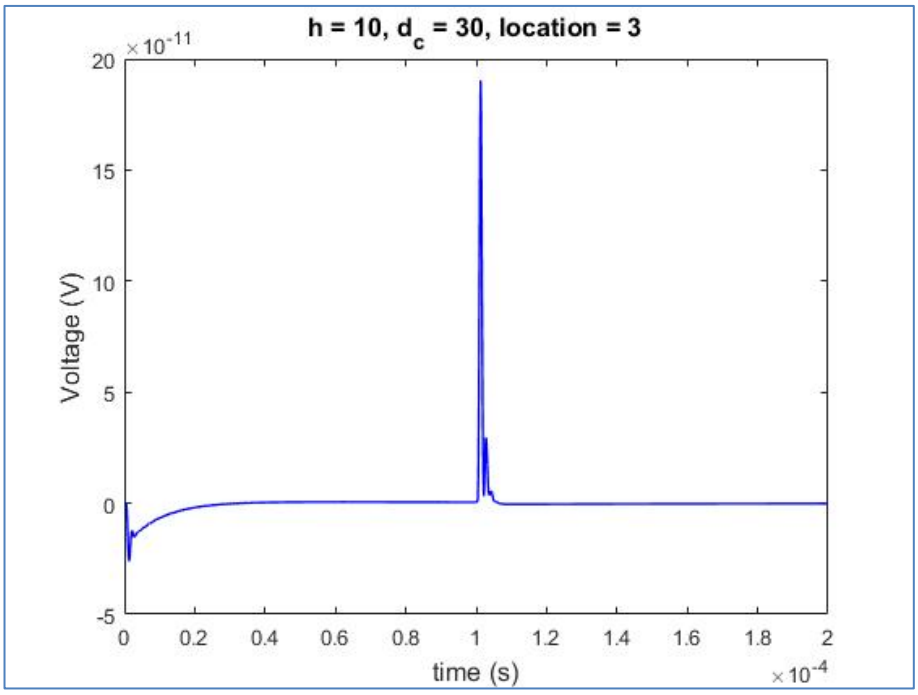

c)

Figure 6.5: Continuation.

6.1.3. Effect of the Horizontal Source Location

The five calculations are made at the five locations of the source on the x axis. The source height h and object depth d_c are 10 cm, both. Figure 6.6 shows that the horizontal location of the source affects only the amplitude of the voltage response, not the decay time. The numerical dispersion caused by the pulse type signal is stronger for the further locations of the sources from the object. It is also seen that location 1, 5 and location 2, 4 have the same results because of the symmetry of the problem geometry. Therefore, it is sufficient to calculate the response only at location 1 and location 2.

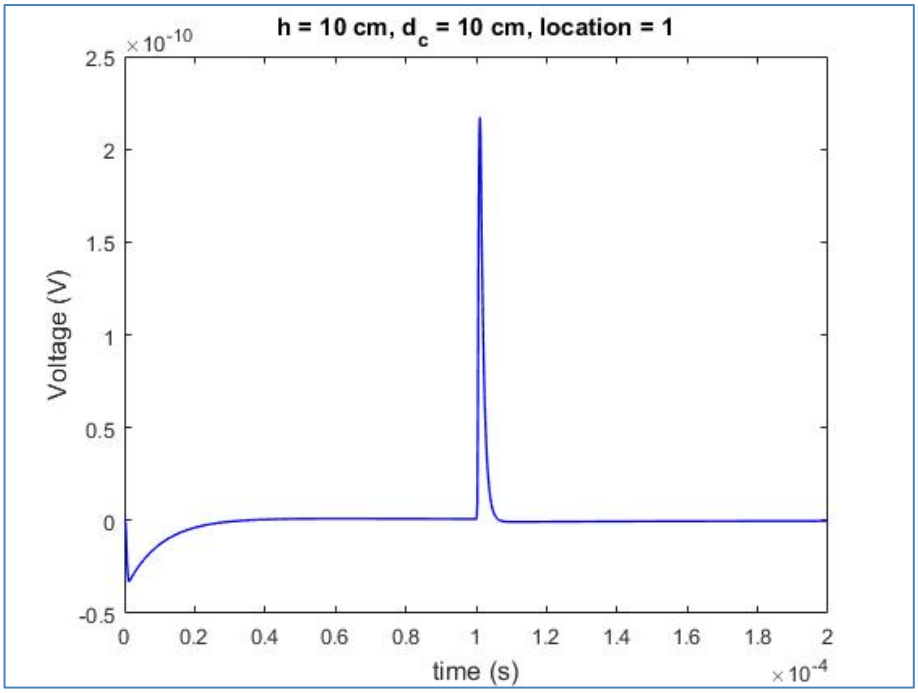

a)

Figure 6.6: The time domain voltage responses for the metal cube at the five horizontal locations.

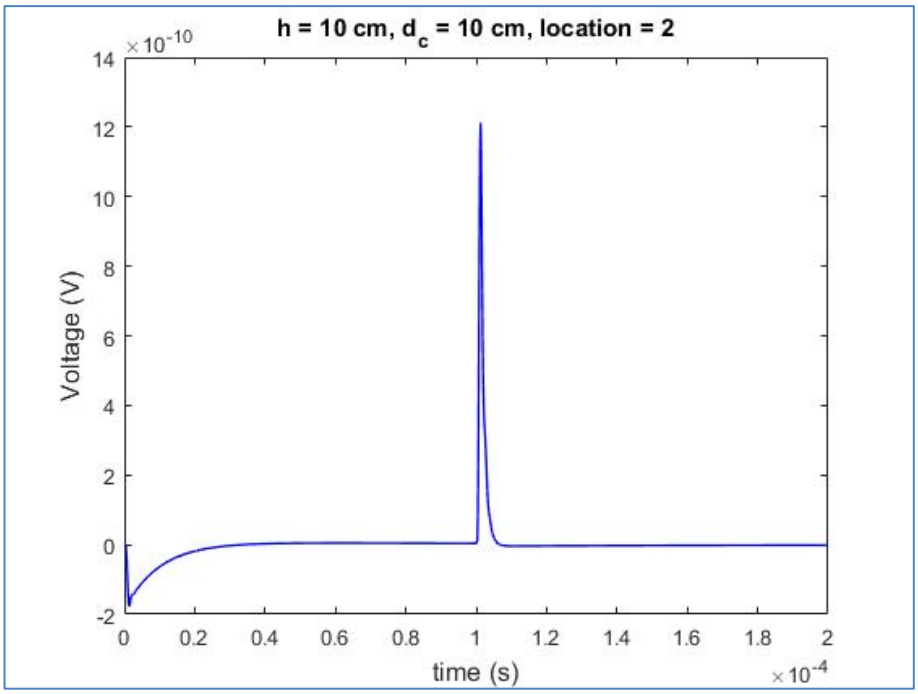

b)

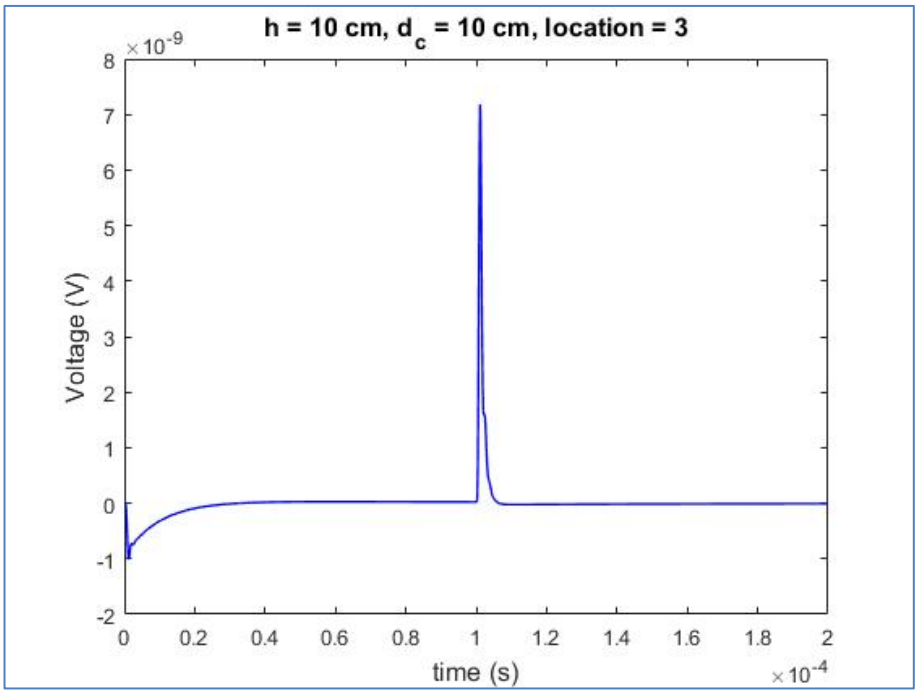

c)

Figure 6.6: Continuation.

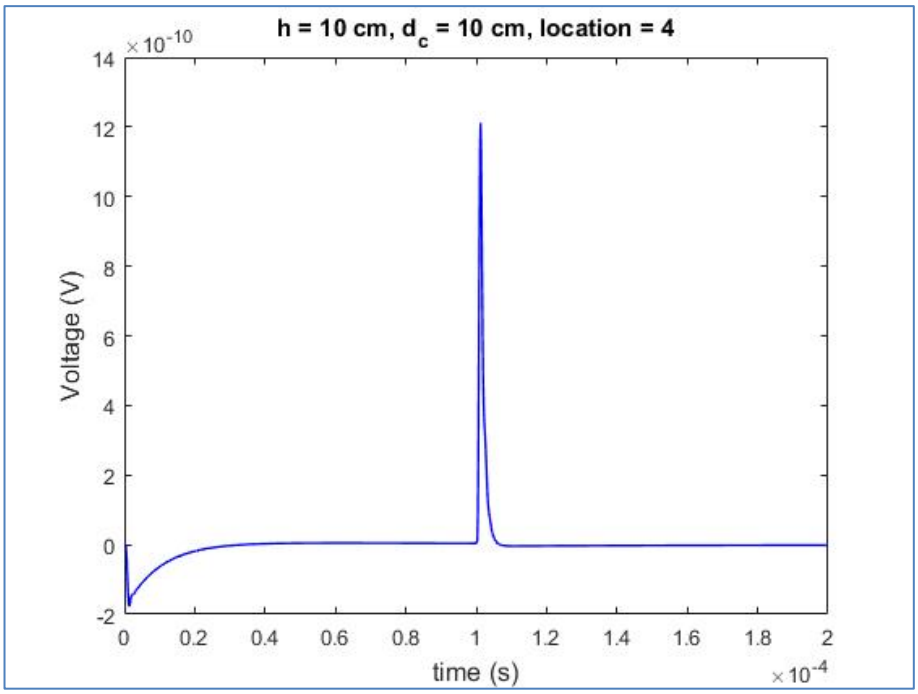

d)

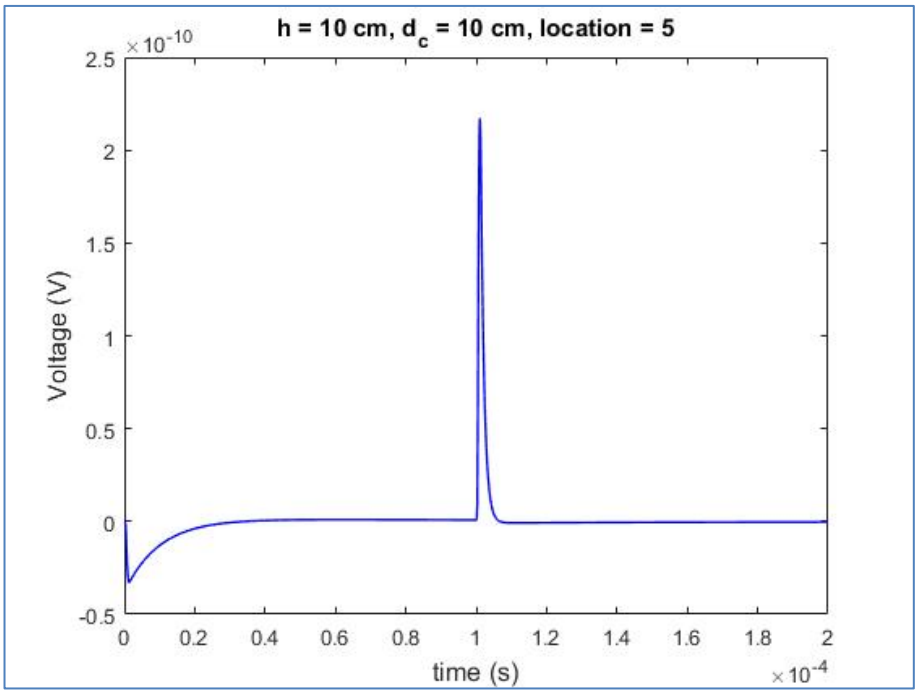

e)

Figure 6.6: Continuation.

6.2. Buried Air Cube

The effects of the source height (h) and the depth of the air filled cube (d_c) are investigated. The side length of the air cube is 0.1 m and located at the middle of the x axis. The calculations are made for the five times at five locations of the source on the x axis ($1, 2, 3, 4$ and 5 locations in Figure 6.1). The time domain data is collected at the same locations.

6.2.1. Effect of the Source Height

In Figure 6.7, the magnetic field strength and voltage in the time domain at location 3 are shown for $h = 10$ cm and $d_c = 20$ cm. The voltage data is obtained by differentiating the magnetic field strength. As seen in Figure 6.7, the very small induced voltage response is obtained from the buried air cube. This makes difficult to analyze its detection.

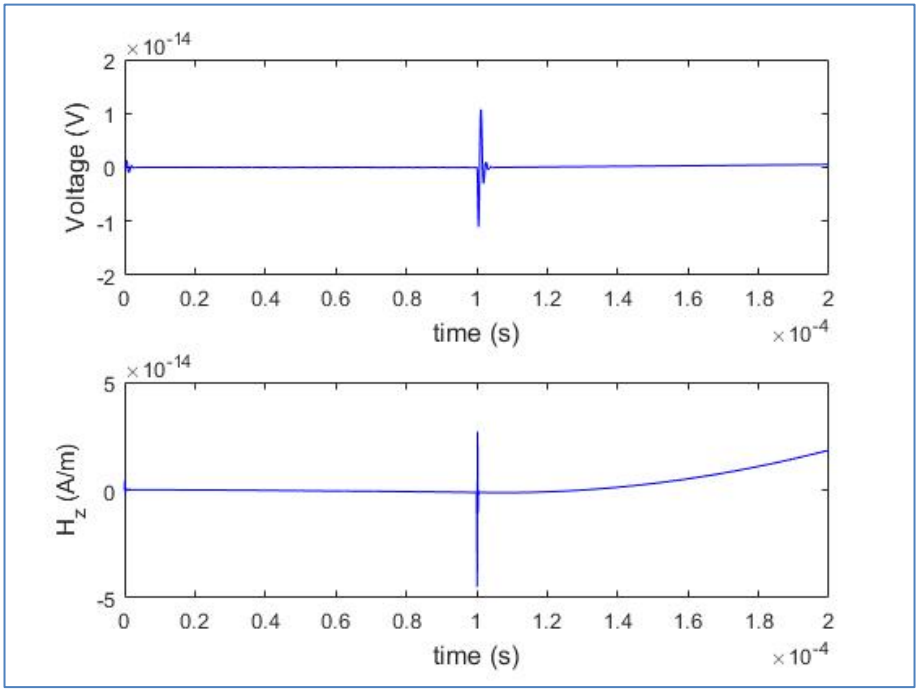

Figure 6.7: The time domain scattered magnetic field (H_z) and voltage response.

The two calculations are made at the two heights of the source $h = 10$ cm and 20 cm for the fixed depth of the buried air cube $d_c = 10$ cm. The source located at

location 3 on the x axis. Figure 6.8 shows that the source height affects only amplitude of the voltage response, not the decay time.

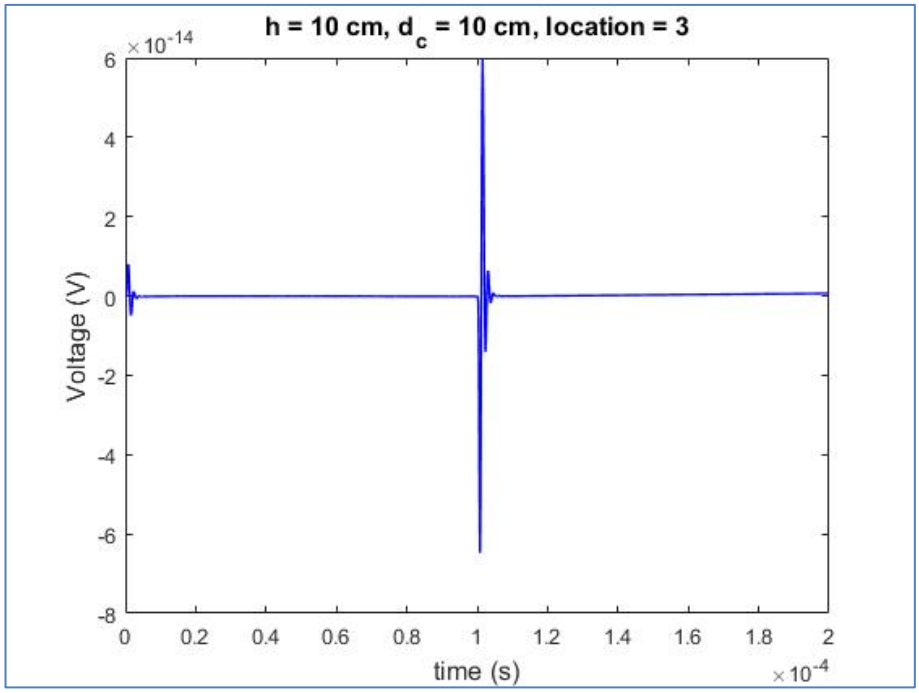

a)

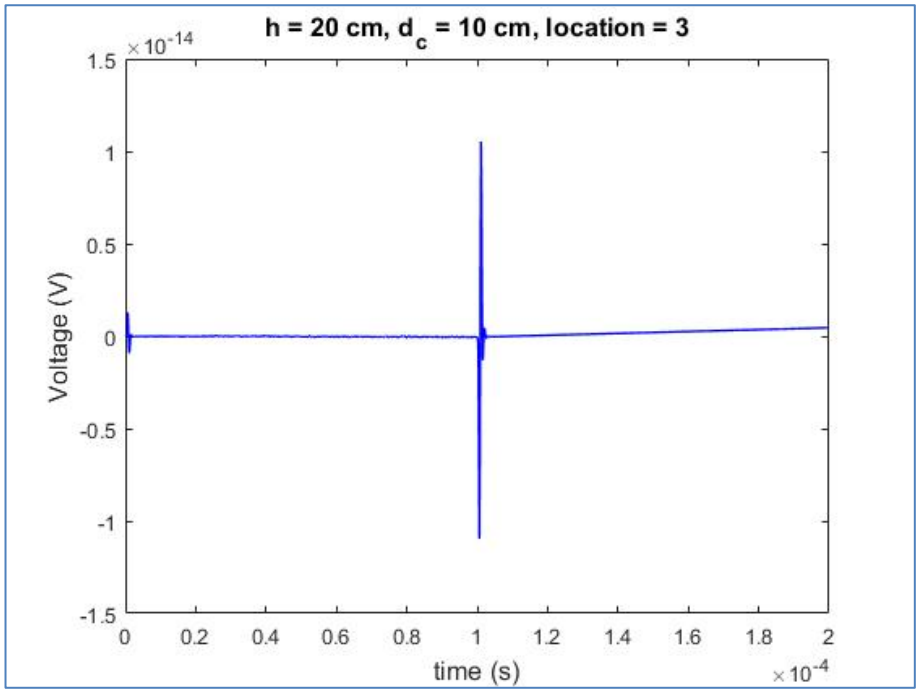

b)

Figure 6.8: The time domain voltage response of the buried air cube at a) $h = 10$ cm and b) $h = 20$ cm.

6.2.2. Effect of the Depth for the Air Cube

Three calculations are made at the three depths for the buried air gap $d_c =$ 10 cm, 20 cm and 30 cm with the fixed height of the source $h = 10$ cm. The source is located at location 3 on the x axis. Figure 6.9 shows that the depth of the air cube affects only the amplitude of the voltage response, not the decay time. The numerical dispersion caused by the pulse type signal is stronger for the deeper buried air cube. Therefore, it is very difficult to filter for obtaining the clear response.

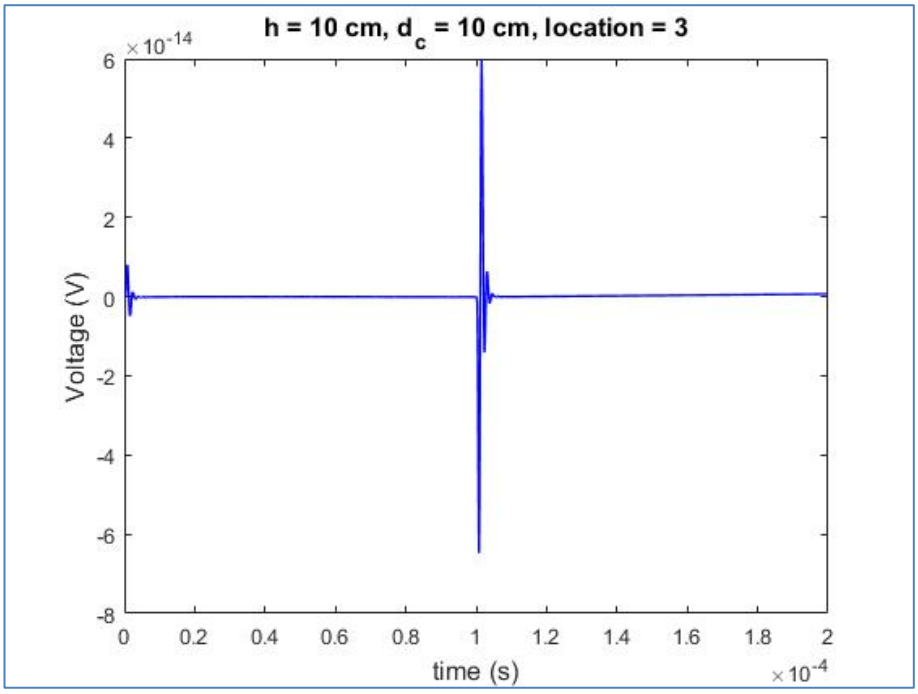

a)

Figure 6.9: The time domain voltage responses for the buried air cube at a) $d_c =$ 10 cm, b) $d_c = 20$ cm and c) $d_c = 30$ cm.

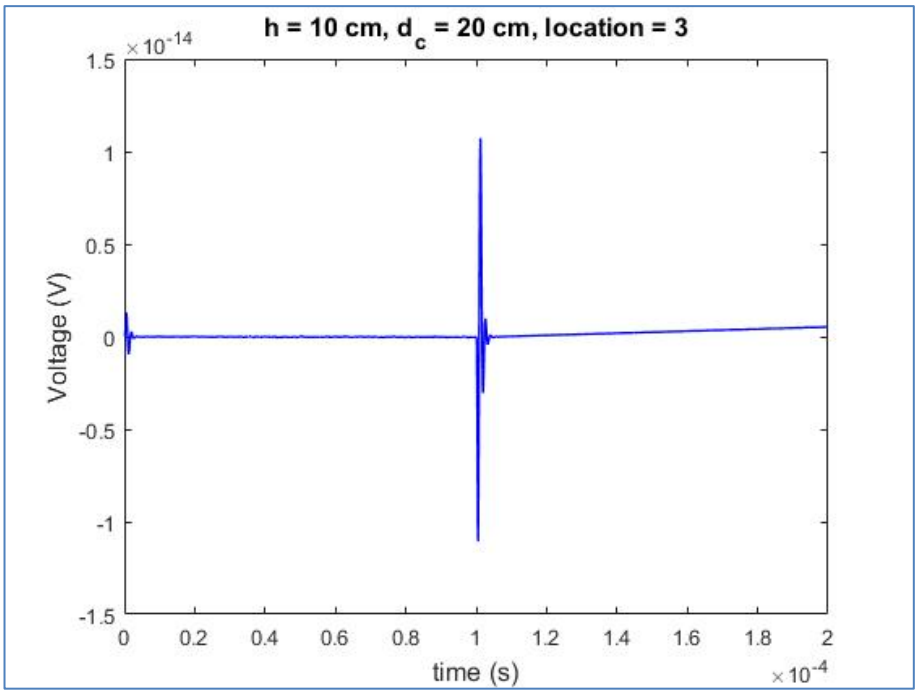

b)

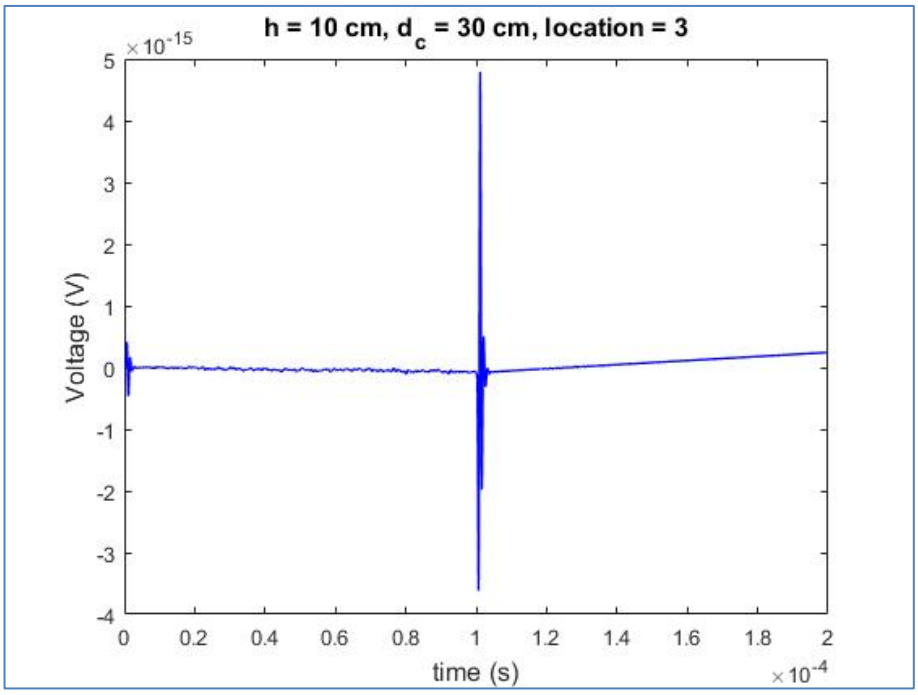

c)

Figure 6.9: Continuation.

6.2.3. Effect of the Horizontal Source Location

Five calculations are made at the five locations of the source on the x axis. The source height h and depth of the air cube d_c are 10 cm, both. Figure 6.10 shows that the horizontal location of the source affects only the amplitude of the voltage response, not the decay time. The numerical dispersion caused by the pulse type signal is stronger for the further locations of the sources from the buried air cube. It is also seen that location 1, 5 and location 2, 4 have the same results because of the symmetry of the problem geometry. Therefore, it is sufficient to calculate the response only at location 1 and location 2.

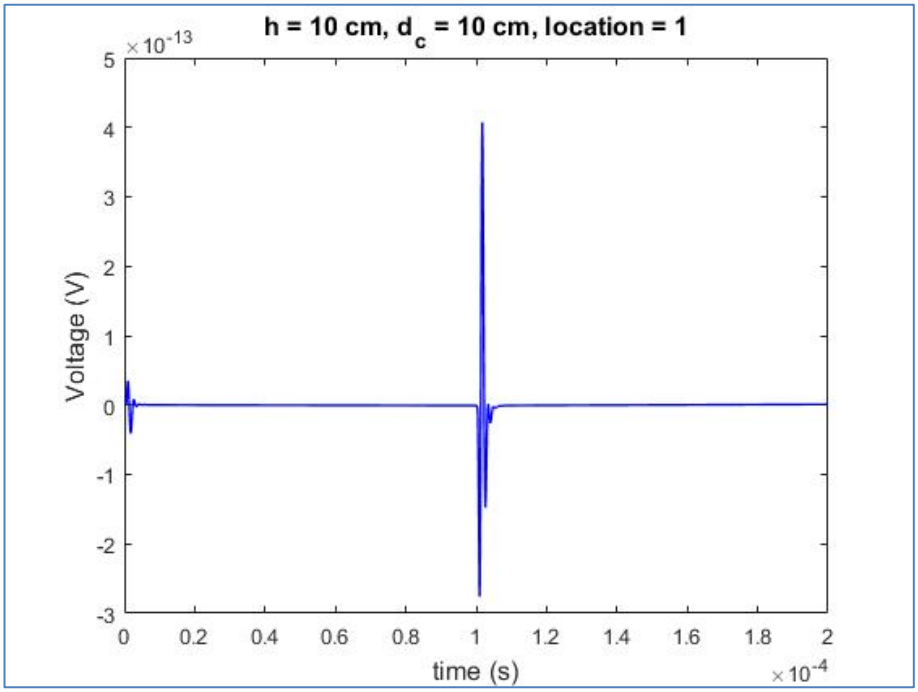

a)

Figure 6.10: The time domain voltage responses for the buried air cube at the five horizontal locations.

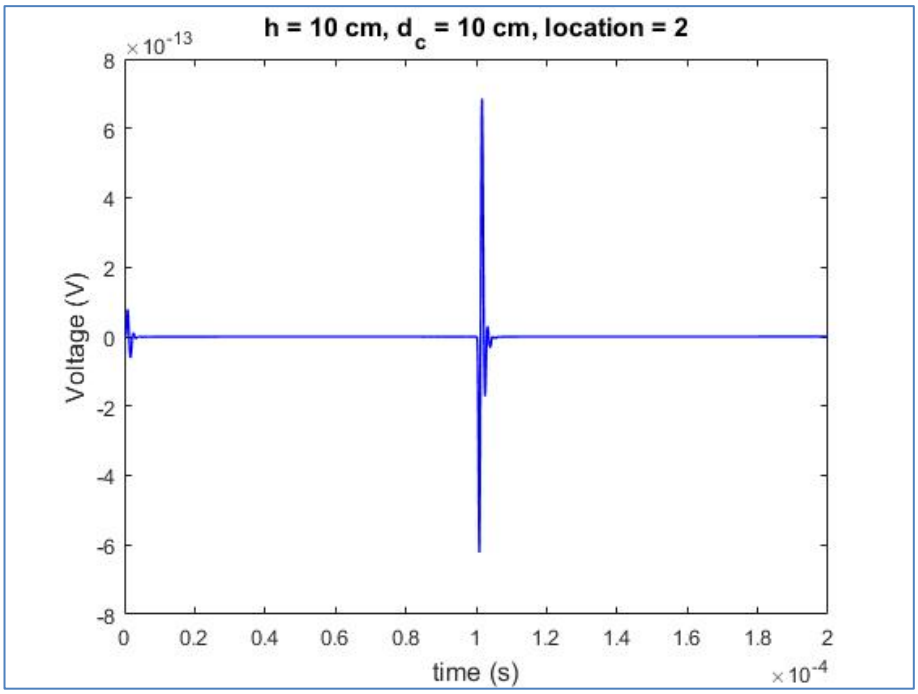

b)

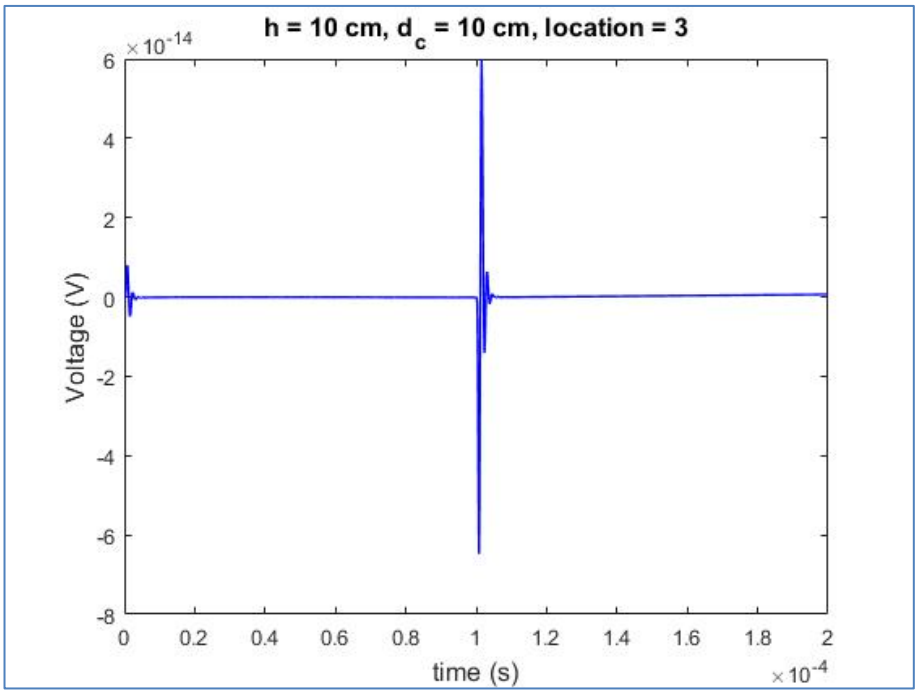

c)

Figure 6.10: Continuation.

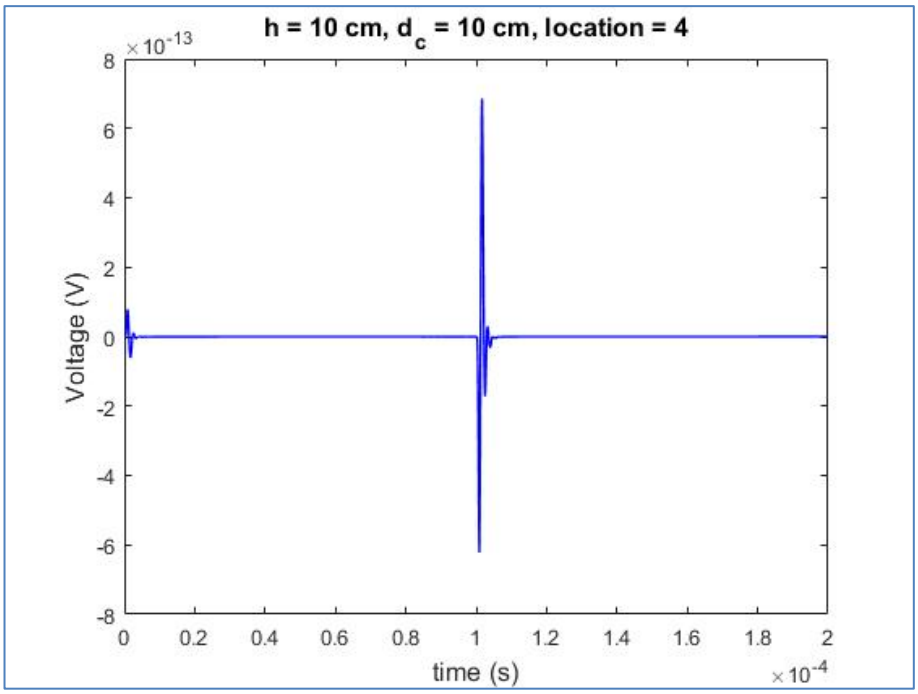

d)

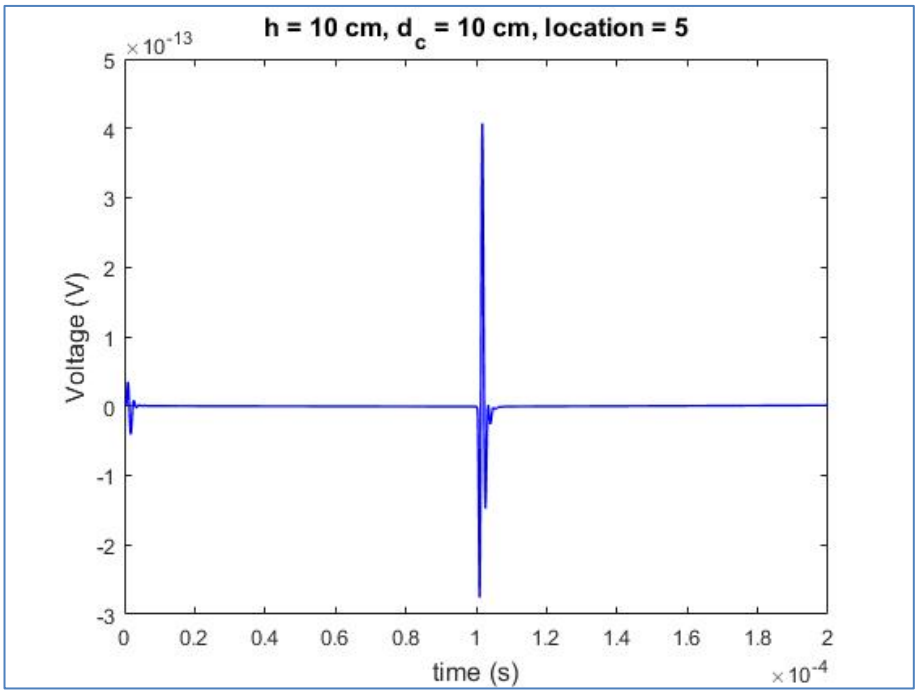

e)

Figure 6.10: Continuation.

6.3. Comparisons of the Results for the Metal and Air Cubes

The results for the buried metal and air cube are compared for the three different scenarios. In Figure 6.11.a, the normalized values of the time domain voltage responses for the antenna height $h = 10$ cm and the object depth $d_c = 10$ cm are shown. The source located at location 3 on the x axis. In Figure 6.11.b, the normalized values of time domain voltage responses for the antenna height $h = 10$ cm and the object depth $d_c = 20$ cm are shown. The source located at location 3 on the x axis. In Figure 6.11.c, the normalized values of time domain voltage responses for the antenna height $h = 10$ cm and the object depth $d_c = 10$ cm are shown. The source located at location 1 on the x axis.

These results show that the time decay curves are significantly different for the buried metal and air cube. The time decay curves for the air cube have oscillations and the amplitude values of the voltage responses are extremely low for detection. These situations make complicated the analysis for the buried air cube. On the other hand, the time decay curves for the metal cube are smooth and its amplitude values are in measurable levels.

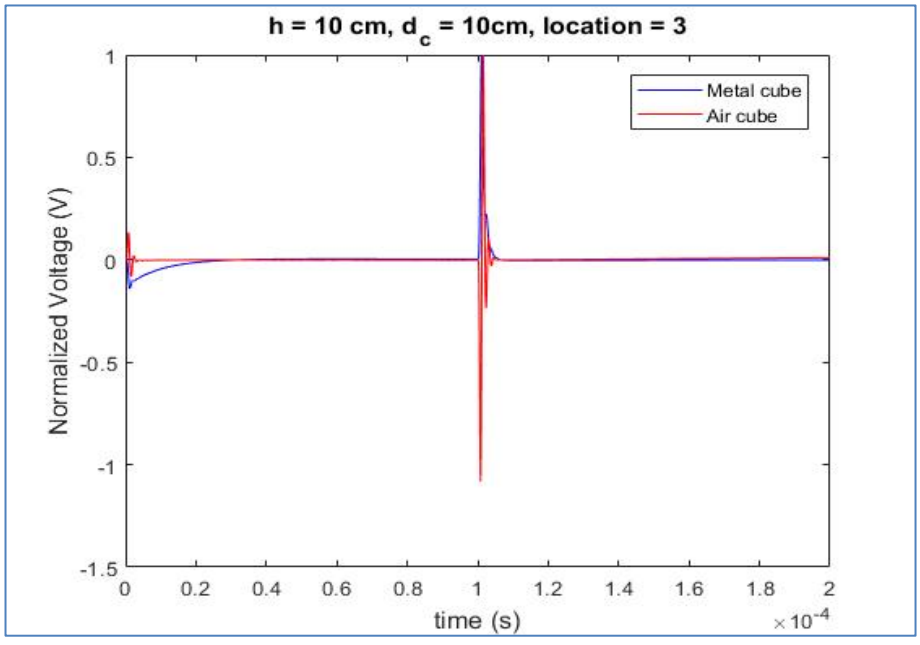

a)

Figure 6.11: The comparisons of the time domain voltage responses of the buried metal and air cube for the three different scenarios.

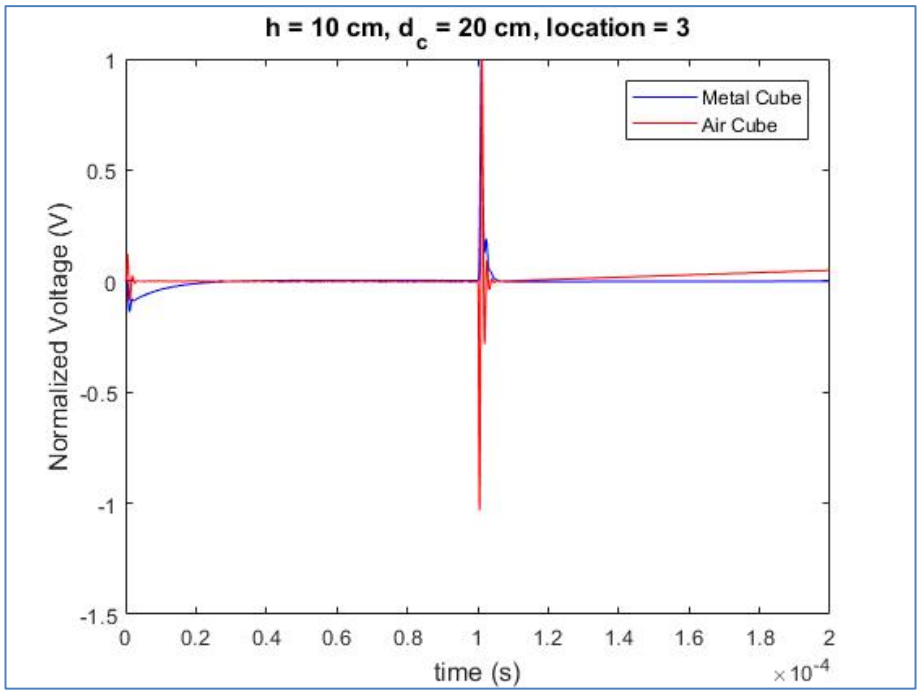

b)

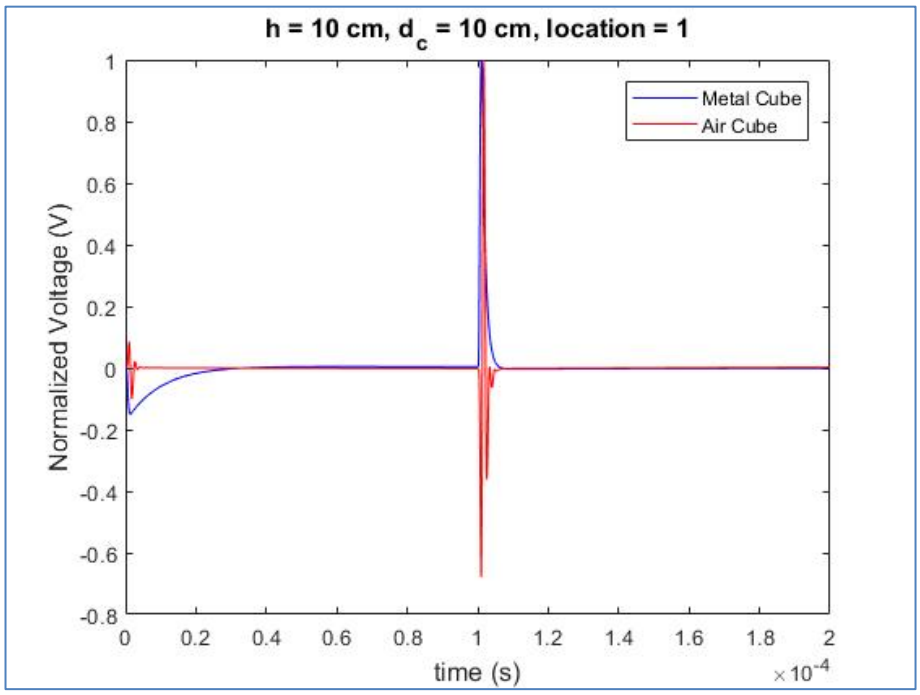

c)

Figure 6.11: Continuation.

7. DISCUSSIONS AND FUTURE WORKS

The QS-FDTD simulation of the pulse induction metal detector is performed in the three dimensional Cartesian coordinates. A magnetic dipole is used as the transmitter antenna. The monostatic configuration is set for the transmitter and receiver antenna placements. The time signatures are obtained for the different scenarios. Therefore, the fundamental knowledge is obtained for the detection and classification of the buried objects.

The effects of the buried object depth, the antenna height and horizontal antenna location on the time signatures were investigated for the buried metal and air cubes. The results show the time decay curves of for the buried metal and air cubes are markedly differed from each other. Therefore, classification for different material types is possible due to time decay curves. It was also clearly observed that the object depth, the antenna height and horizontal antenna location simply affect the amplitude of the received signal. It can also be concluded that the detection and discrimination of the buried air cube very difficult. This is because of its extremely low voltage response.

There are also potential future works to be investigated:

- Time signatures of the different soils,
- Effects of the object shape, the material type, the object orientation, the source type etc.,
- Time signatures of buried magnetic objects,
- Ground compensation possibilities,
- Effects of magnetic dispersive soils on the received signal.

REFERENCES

Aksoy S., (2017), “Zaman Uzayı Sonlu Farklar Yöntemi – Ders Notları”, Electronics Engineering Department, Gebze Technical University, Gebze, Kocaeli.

Aksoy S., (2018), “Advanced Metal Detectors”, http://anibal.gyte.edu.tr/dosya/102/~saksoy/Metal%20Detectors/Advanced%20Metal%20Detectors.html.

Ambruš D., Vasić D., Bilas V., (2016), “Estimating directional magnetic polarizabilities of metallic objects using planar time-domain electromagnetic induction sensor”, Sensors Applications Symposium (SAS), April 20-22, Catania, Italy.

Antoun C. A., Perriard Y., (2013), “Robust and efficient 3D model of an electromagnetic induction (EMI) sensor”, IEEE International Conference on Electrical Machines and Systems, 831-836, October 26-29, Busan, Korea.

Arabi A. R., Mittra R., (1995), “An alternate form of the MUR second-order absorbing boundary condition”, Microwave and Optical Technology Letters, 9-6, 336-338.

Balanis C. A., (2005), “Antenna Theory Analysis and Design”, 3rd Edition, John Wiley and Sons.

Barrowes B. E., Shubitidze F., Fernandez P., Shamatava I., O’Neill K., (2009), “Men-portable vector EMI instrument data characterization using the NSMS method”, Proceedings of the SPIE, 7303-13.

Bowler J. R., (1990), “Prediction and analysis of transient eddy-current probe signals”, Review of Progress in Quantitative Nondestructive Evaluation, 9, 287-293.

Bowler J., Johnson M., (1997), “Pulsed eddy-current response to a conducting half-space”, IEEE Transactions on Magnetics, 33-3, 2258-2264.

Chilaka S. V., Faircloth D. L., Riggs L. S., Baginski M. E., (2005), “A comparison of discrimination capabilities of time- and frequency-domain electromagnetic induction systems”, Proceedings of the SPIE, 5794, 242-253.

Chou W., Matsumoto R., Tajima F., (2000), “Simulational modeling of time-domain magnetic induction using parallel computational schemes (I) in the Cartesian coordinates”, Computer Physics Communications, 131-1, 26-40.

Chou W., Matsumoto R., Tajima F., (2001), “Simulational modeling of time-domain magnetic induction using parallel computational schemes (II) in the Cartesian coordinates”, Computer Physics Communications, 181-2, 175-191.

Chu S. T., Huang W.P., Chaudhuri S.K., (1991), Simulation and analysis of waveguide based optical integrated circuits, Computer Physics Communications, 68, 451-484.

Colani C., (1966), “A new type of locating device. I – The instrument”, Archaeometry, 9-1, 3-9.

Colani C., Aitken M. J., (1966), “A new type of locating device. II – Field trials”, Archaeometry, 9-1, 9-19.

Das Y., McFee J. E., Chesney R. H., (1984), “Time domain response of a sphere in the field of a coil: Theory and experiment”, IEEE Transaction on Geoscience and Remote Sensing, 22-4, 360-367.

Das Y., McFee J. E., Chesney R. H., (1984), “Determination of depth of shallowly buried objects by electromagnetic induction”, IEEE Transaction on Geoscience and Remote Sensing, 23-1, 60-66.

Das Y., (2004), “A preliminary investigation of the effects of soil electromagnetic properties on metal detectors”, Detection and Remediation Technologies for Mines and Minelike Targets IX.

Das Y., (2006), “Time-domain response of a metal detector to a target buried in soil with frequency-dependent magnetic susceptibility”, Detection and Remediation Technologies for Mines and Minelike Targets XI, Proceeding of SPIE, 6217, 621701-1:5, 17-21 April, Kissimmee, Florida, USA.

Davey K. R., Han H. C., (1987), “An integral eigenvalue approach to three-dimensional field problems--A low-frequency variation of SEM”, IEEE Journal of Oceanic Engineering, 12-2, 466-475.

Dyck D. N., Gilbert G., Forghani B., Webb J. P., (2004), “An NDT pulse shape study with TEAM Problem 27”, IEEE Transaction on Magnetics, 40-2, 1406-1409.

Fernandez J. P., Barrowes B. E., Grzegorczyk T. M., LHomme N., O’Neill K., Shubitidze F., (2011), “A man-portable vector sensor for identification of unexploded ordnance”, IEEE Sensors Journal, 11-10, 2542-2555.

Fernandez J. P., Barrowes B. E., Bijamov A., Grzegorczyk T. M., LHomme N., O’Neill K., Shamatava A., Shubitidze F., (2011), “MPV-II: an enhanced vector man-portable EMI sensor for UXO identification”, Proceedings of the SPIE, 8017.

Hamano Y., (2002), “A new time-domain approach for the electromagnetic induction problem in a three-dimensional heterogeneous earth”, Geophysical Journal International, 150-3, 753-769.

Jiracek G. R., “Transient Electromagnetic Soundings "Abridged Notes"”, Department of Geological Sciences, San Diego State University.

Karmis P., Papadopoulos T., Louis I. F., (2003), “Applicability study of coincident loop transient EM soundings”, Journal of the Balkan Geophysics Society, 6-2, 88-100.

Kim B., Lee S., Han S. H., Kim K., (2014), “Magnetic sheet backed search coil for pulsed-induction metal detector system”, Electronics Letters, 50-23, 1704-1706.

Ludwig R., Dai X. W., (1990), “Numerical and analytical modeling of pulsed eddy currents in a conducting half-space”, IEEE Transaction on Magnetics, 26-1, 299-307.

Mackie R. L., Madden T. R., Wannamaker P. E., (1993), “Three-dimensional magnetotelluric modeling using difference equations – theory and comparisons to integral equation solutions”, Geophysics, 58-2, 215-226.

McFee J. E., Chesney R. H., Das Y., Toews J., Turnbull M., Pinnel R., Bell M., (1984), “Experimental time domain electromagnetic induction system, Review of Scientific Instruments”, 55-6, 968-975.

Mogilatov V., Goldman M., Persova M., Soloveichik Y., (2014), “Displacement currents in geoelectromagnetic problems, Journal of Applied Geophysics”, 105, 133-137.

Mur G., (1981), “Absorbing boundary conditions for the finite-difference approximation of the time-domain electromagnetic-field equations”, IEEE Transaction on Electromagnetic Compatibility, 23-4, 377-382.

Nabighian M. N., (1979), “Quasi-static transient response of a conducting half-space – an approximate representation”, Geophysics, 44-10, 1700-1705.

Nabighian M. N., (1979), “Quasi-static transient response of a conducting half-space – an approximate representation”, Geophysics, 44-10, 1700-1705.

Nelson C. V., Arabian A. K., (2002), “Low-cost backpack-portable robot system for mine and UXO detection and identification”, Proceedings of the SPIE, 4742, 574-582.

Özakın M. B., Aksoy S., (2016), “Application of magneto-quasi-static approximation in the finite difference time domain method”, IEEE Transaction on Magnetics, 52-8, 7209809.

Özakın M. B., Aksoy S., (2017), “Numerical calculation of the magnetic dipole fields by three-dimensional QS-FDTD method”, Progress in Electromagnetic Research Symposium, 22-25 May, St Petersburg, Russia.

Raiche A. P., Spies B. R., (1981), “Coincident loop transient electromagnetic master curves for interpretation of two-layer earths”, Geophysics, 46-1, 53-64.

Riggs L. S., Cash S., Bell T., (2002), “Progress toward an electromagnetic induction mine discrimination system”, Proc. SPIE, 4742, 736-745.

Ripka P., Lewis A., (2006), “Eddy current metal detectors – pulse vs. CW”, Journal of Electrical Engineering, 57-8, 175-177.

Ripka P., Vcelak J., Kaspar P., Lewis A. M., (2006), “Bomb detection in magnetic soils: AC versus DC methods”, IEEE Sensors, EXCO, 22-25 October, Daegu, Korea.

Sebak A. A., Shafai L., (1984), “Transient response computation of spheroidal objects using impedance boundary conditions”, IEEE Transaction on Antenna and Propagation, 32-10, 1116-1122.

Sebak A. A., Shafai L., Das Y., (1988), “Electromagnetic transient response of rotationally symmetric permeable conducting objects”, IEEE Antennas and Propagation Society Int. Symposium, 3, 1044-1047.

Song L. P., Shubitidze F., Pasion L. R., Oldenburg D. W., Billings S. D., (2008), “Computing transient electromagnetic responses of a metallic object using a spheroidal excitation approach”, IEEE Geoscience and Remote Sensing Letters, 5-3, 359-363.

Shubitidze F., Fernandez J. P., Barrowes B. E., Shamatava I., Bijamov A., O’Neill K., Karkashadze D., (2014), “The orthonormalized volume magnetic source model for discrimination of unexploded ordnance”, IEEE Transaction Geoscience and Remote Sensing, 52-8, 4658-4670.

Shubitidze F., Barrowes B. E., Wang Y., Shamatava I., Sigman J. B., O’Neill K., Steinhurst D. A., (2016), “A high power EMI sensor for detecting and classifying small and deep targets”, Proceedings of the SPIE, 9823, 982308 11pp.

Singh S. K., (1973), “Electromagnetic transient response of a conducting sphere embedded in a conductive medium”, Geophysics, 38-5, 864-893.

Taflove A., Hagness S. C., (2005), “Computational Electrodynamics: The Finite-Difference Time-Domain Method”, 3rd Edition, Boston, MA: Artech House.

Tsuboi H., Seshima N., Sebestyen I., Pavo J., Gyimthy S., Gasparics A., (2004), “Transient eddy current analysis of pulsed eddy current testing by finite element method”, IEEE Transaction on Magnetics, 40-2, 1330-1333.

Uyeshima M., Schultz A., (2000), “Geomagnetic induction in a heterogeneous sphere: a new three-dimensional forward solver using a conservative staggered-grid finite difference method”, Geophysical Journal Int., 140-3, 636-650.

Verma R. K., Mallick K., (1979), “Detectability of intermediate conductive and resistive layers by time-domain electromagnetic sounding”, Geophysics, 44-11, 1862-1878.

Wait J. R., (1951), “A conducting sphere in a time varying magnetic field”, Geophysics, 16, 666-672.

Wait J. R., (1953), “A transient magnetic dipole source in a dissipative medium”, Journal of Applied Physics, 24-3, 341-343.

Wait J.R., Spies K. P., (1969), “Quasi-static transient response of a conducting permeable sphere”, Geophysics, 34-5, 789-792.

Wait J. R., Ott R. H., (1972), “On calculating transient EM fields of a small current-carrying loop over a homogeneous earth”, Pageoph, 95-1, 157-162.

Xie S., Chen Z., Takagi T., Uchimoto T., (2011), “Efficient numerical solver for simulation of pulsed eddy-current testing signals”, IEEE Transaction on Magnetics, 47-11, 4582-4591.

Yee K. S., (1966), “Numerical solution of initial boundary value problems involving Maxwell’s equations in isotropic media”, IEEE Transaction on Antennas and Propagation, 14-3, 302-307.

Yang P., Liou K. N., (1998), “An efficient algorithm for truncating spatial domain in modeling light scattering by finite-difference technique”, Journal of Computational Physics, 140-2, 346-369.

Yusheng z., Wenbing W., (1996), “The studies of the stability of FDTD with Mur’s absorbing boundary condition of second order in 3-D scattering problems”, IEEE Microwave and Guided Wave Letters, 6-3, 120-122.

BIOGRAPHY

Talha SAYDAM was born in Sivas in 1993. He received his bachelor degree in Gebze Technical University, Graduate School of Natural and Applied Sciences, Electronic Engineering Department in 2016. He currently works at Department of Electronics Engineering, Gebze Technical University as a research assistant. His research areas are about numerical time domain electromagnetics at the low frequencies.